This is to certify that the
thesis entitled

THE EFFECTS OF COULOMB FRICTION ON THE
PERFORMANCE OF CENTRIFUGAL PENDULUM
VIBRATION ABSORBERS

presented by

BRENDAN JAMES VIDMAR

has been accepted towards fulfillment
of the requirements for the

M.S. degree in Mechanical Engineering

Brian Feeny
Major Professor's Signature

8/24/09
Date

THE EFFECTS OF COULOMB FRICTION ON THE PERFORMANCE OF CENTRIFUGAL PENDULUM VIBRATION ABSORBERS

By

Brendan James Vidmar

A THESIS

Submitted to
Michigan State University
in partial fulfillment of the requirements
for the degree of

MASTER OF SCIENCE

Mechanical Engineering

2009

ABSTRACT

THE EFFECTS OF COULOMB FRICTION ON THE PERFORMANCE OF CENTRIFUGAL PENDULUM VIBRATION ABSORBERS

By

Brendan James Vidmar

In this work, the effects of damping parameters, specifically Coulomb friction, on the performance of centrifugal pendulum vibration absorbers (CPVAs) is investigated analytically and experimentally. The full non-linear equations of motion for a rotor subjected to an engine order applied torque and equipped with a circular path CPVA are non-dimensionalized and scaled with the inclusion of viscous and Coulomb damping, and the perturbation technique of averaging is applied to the scaled equations. The absorber dynamics and corresponding angular acceleration of the rotor are investigated theoretically and a "jump" bifurcation is observed under certain loading and parameter conditions. To quantify values for the viscous and Coulomb damping parameters in the experimental rig, a simultaneous decrement method is recast to account for noise and low resolution in the experimental rig and then applied to experimental data. It is shown that using this decrement scheme, the damping parameters can be estimated to a high degree of accuracy. Finally, experimental results and simulations of the full non-linear equations are presented and shown to be in good agreement with results from the averaging theory. The hysteresis phenomenon and jump bifurcation of absorber amplitude is observed experimentally. This system instability, which causes the absorbers to jump to large amplitudes, is shown analytically and experimentally to significantly increase the vibrations of the rotor, and must be avoided in practice. The results derived here will be of general use in assessing absorber performance when dry friction is present in the absorber suspension.

DEDICATION

To my parents

ACKNOWLEDGMENT

Many people have helped me tremendously during my time completing this thesis. Special thanks goes to my triad of advisors, Drs. Feeny, Shaw, and Haddow. Dr. Feeny has been a joy to work with, always welcoming my many questions or just chatting. System identification is a very important area of engineering and I have gained a lot of knowledge from him in this area. Dr. Shaw is man of immense knowledge and I hope no one knows more about CPVA's than him (for their own good). And last, but not least, Dr. Haddow has spent countless hours assisting me in the experimentation and his knowledge of experimental techniques has taught me a lot. Ryan Monroe, another graduate student working on CPVAs, has been a tremendous help, allowing me to bounce my ideas off him, and then showing me how I was usually wrong! I would also like to thank my other lab mates, Nick Miller, Stephanie Frangakis, and Thomas Theisen for making this experience an enjoyable one as well as their help in this work.

TABLE OF CONTENTS

LIST OF TABLES

LIST OF FIGURES

Chapter 1

Introduction

The jet engine that makes intercontinental flight possible, the internal combustion engine which revolutionized ground transportation, the turbines that provide power to a city, and the helicopter rotor which permits the operator to hover and fly as he pleases are all subjected to rotating torques that are a function of the angle of rotation. In many cases these torques can cause unwanted or even dangerous torsional vibrations of the system at hand.

Centrifugal pendulum vibration absorbers (CPVAs) have been shown to significantly reduce torsional vibrations in rotating machinery that arise from engine order excitation [1,3–5,9]. Such machinery includes internal combustion engines, helicopter rotors, turbines, and rotary aircraft engines as previously mentioned. CPVAs have been used for several decades in light aircraft engines and helicopter rotors [6]. Figure 1.1 shows bifilar CPVAs attached to a helicopter rotor in order to decrease torsional vibrations of the driveshaft.

Previous use of CPVAs in aerospace applications has been to reduce torsional vibrations of a rotor operating at a nearly constant angular velocity. Recent research has been conducted into the response and corresponding effectiveness of CPVAs for use in automotive applications where the mean speed of the rotor varies greatly

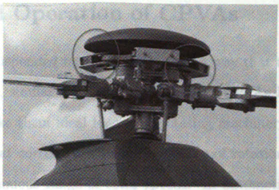

Figure 1.1: Bifilar Absorbers on a Helicopter Rotor. (http://www.b-domke.de /AviationImages/Rotorhead/11358.html)

throughout the range of operation [13, 14]. A crankshaft used in an automotive engine fitted with CPVAs is shown in Figure 1.2.

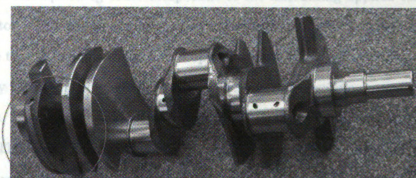

Figure 1.2: Circular Path CPVA on Automotive Crankshaft.

CPVAs have recently come to the forefront in the automotive industry to reduce torsional vibrations in multi-displacement engines, which are designed to achieve greater fuel economy. In this day and age of ever increasing demand for greater fuel economy, CPVAs could turn out to be an important tool.

1.1 General Operation of CPVAs

CPVAs are masses suspended from a rotor in such a way that they are free to move along a desired path, similar to that of a pendulum. CPVAs have several inherent properties which make them ideal for use in rotating machinery. First, they have a natural frequency that corresponds to a given order of rotation, thus making them effective over a continuous range of rotor speeds. In automotive applications, this order is a function of the number of cylinders being used. In a four stroke internal combustion engine, each cylinder has a cycle of two rotations, or a period of 4π radians. Thus, an N cylinder engine will have a leading order harmonic at order $\frac{N}{2}$. With this knowledge, we can model the forcing from a four stroke internal combustion as $T\sin(n\theta)$, where the forcing order, n is equal to $N/2$.

When tuned to the correct order, the absorbers oscillate in a manner that counteracts the corresponding order component of the fluctuating applied torque acting on the rotor. This works similar to the tuned translational absorber, and has the advantage that it remains tuned for all operating conditions. In addition, CPVAs are completely passive devices which require no active control scheme to reduce torsional vibrations. Lastly, these devices dissipate very little energy, and are thus very energy efficient. The little energy the pendulums do dissipate, though, has a significant effect the performance of the CPVA.

1.2 Contributions

Den Hartog [5] first considered the non-linearities associated with circular path CPVAs and investigated the undesired effects the large pendulum amplitude instability has on the absorber's performance. Newland [10] expanded on Hartog's idea of overtuning the pendulums in order to avoid this dangerous instability and developed a set of guidelines to follow when choosing the tuning order. Madden's patent on

cycloidal paths [8] started research into alternative paths that help deal with the non-linearities. Denman [4] explored more paths and tested absorbers with these special paths in an automotive engine. Nester [9] theoretically and experimentally investigated the steady-state circular path absorber response with an equivalent viscous damping model. This work extends on Nester's investigation by incorporating a Coulomb friction term into the equations of motion. The equations of motion are then averaged with the inclusion of the Coulomb friction term and the corresponding performance of the absorber is theoretically investigated.

In order to accurately quantify the viscous and Coulomb damping parameter in an experimental rig, a simultaneous viscous/Coulomb decrement method is recast to account for noise and low resolution in the experimental device. Results are presented that this method can accurately predict the damping in the system.

Finally, experimental results are presented that show the responses predicted by theory are correct for a single absorber.

1.3 Outline of Thesis

Once the reader has been introduced to the general features and operation of CPVAs, some detailed analysis will be conducted and results presented.

In Chapter Two, the non-linear equations of motion for a rotor equipped with a single circular path absorber will be derived, non-dimensionalized and scaled so as to be in a form in which the common perturbation technique of averaging can be applied. After the equations have been averaged, some analysis is conducted into the performance of a single absorber on a rotor. More specifically, the stability and performance of the absorber is investigated for different absorber parameters, as well as the corresponding effect it has on the angular acceleration of the rotor.

In the third chapter, the experimental rig used for testing is introduced. Next, the

physical parameters associated with the rig are identified via different experimental techniques. These parameters include the rotor inertia, absorber inertia, absorber tuning order, and absorber damping. In regards to the absorber damping, a simultaneous viscous/Coulomb decrement method is improved upon to correctly identify the damping parameters.

Chapter Four presents experimental results corresponding to the theory developed in Chapter Two. The absorber amplitude and corresponding angular acceleration of the rotor versus applied torque are experimentally measured and compared against theory.

Finally, Chapter Five discusses the conclusions based on the work in the previous chapters, as well as some recommendations for future research.

Chapter 2

Theoretical Investigation

2.1 CPVA Equations of Motion

The equations of motion for a rotor equipped with a single CPVA will be derived. A Coulomb friction term will be introduced and its effects on the performance of the absorber will be presented. We start with a complete derivation of the equations of motion, then non-dimensionalize these equations, scale them and perform averaging on the scaled versions. Graphical results are presented and will be compared to experimental results in Chapter 4.

A picture of a circular path CPVA investigated is shown in Figure 2.1 and the corresponding schematic with labeled unit vectors and parameters is shown in Figure 2.2.

Table 2.1 defines the parameters given in Figure 2.2. To develop the equations of motion we will formulate kinetic and potential energies as well as the generalized forces and apply Lagrange's method.

A position vector to the absorber's center of mass (COM) can be written as

$$\vec{r} = R\hat{e}_R + L\hat{e}_r.$$

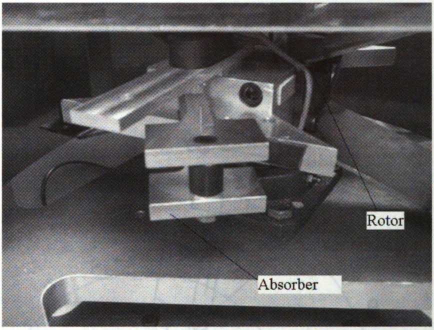

Figure 2.1: A Circular Path Absorber Shown Mounted to a Rotor.

Table 2.1: Definition of Symbols in Figure 2.2.

Symbol	Physical Meaning
θ	Rotor angle
ϕ	Absorber's swing angle with respect to the rotor
R	Distance from the rotor center to the absorber's center of rotation
L	Distance from the absorber's center of rotation to its center of mass
0	Center of rotor
c	Location of the absorber's center of mass
A	Point about which the absorber swings

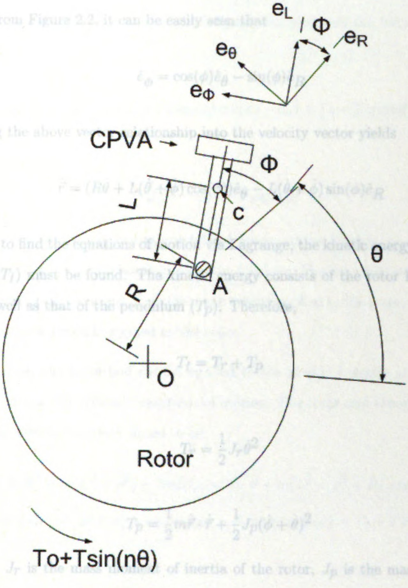

Figure 2.2: Schematic of Rotor and CPVA for Deriving the Equations of Motion.

Taking a time derivative produces a velocity vector

$$\dot{\vec{r}} = R\dot{\theta}\hat{e}_{\theta} + L(\dot{\theta} + \dot{\phi})\hat{e}_{\phi}$$

where, from Figure 2.2, it can be easily seen that

$$\hat{e}_{\phi} = \cos(\phi)\hat{e}_{\theta} - \sin(\phi)\hat{e}_{R}$$

Plugging the above vector relationship into the velocity vector yields

$$\dot{\vec{r}} = (R\dot{\theta} + L(\dot{\theta} + \dot{\phi})\cos(\phi))\hat{e}_{\theta} - L(\dot{\theta} + \dot{\phi})\sin(\phi)\hat{e}_{R} \tag{2.1}$$

In order to find the equations of motion via Lagrange, the kinetic energy of the entire system (T_t) must be found. The kinetic energy consists of the rotor kinetic energy (T_r) as well as that of the pendulum (T_p). Therefore,

$$T_t = T_r + T_p$$

where

$$T_r = \frac{1}{2}J_r\dot{\theta}^2$$

and

$$T_p = \frac{1}{2}m\dot{\vec{r}}\cdot\dot{\vec{r}} + \frac{1}{2}J_p(\dot{\phi} + \dot{\theta})^2$$

in which J_r is the mass moment of inertia of the rotor, J_p is the mass moment of inertia of the pendulum about its center of mass and m is the mass of the pendulum. Grouping all the terms, letting $J_p = m\rho^2$ where ρ is the pendulum's radius of gyration

about its center of mass, and performing the dot product gives

$$T_t = \frac{1}{2}J_r\dot{\theta}^2 + \frac{1}{2}m\left[R^2\dot{\theta}^2 + 2RL\dot{\theta}(\dot{\theta}+\dot{\phi})\cos(\phi) + L^2(\dot{\theta}+\dot{\phi})^2 + \rho^2(\dot{\theta}+\dot{\phi})^2\right]$$

Next, the generalized forces, which include the damping and the forcing terms, can be found to be

$$Q_\theta = c_a\dot{\phi}\cos(\phi) + F_s\mathrm{sgn}(\dot{\phi})\cos(\phi) - c_o\dot{\theta} + T_o + T\sin(n\theta)$$

for the rotor, and

$$Q_\phi = -c_a\dot{\phi} - F_s\mathrm{sgn}(\dot{\phi})$$

for the absorber. Terms in the generalized forces are as follows: c_a is the viscous damping in the pendulum bearing, F_s is the Coulomb friction in the pendulum bearing, c_o is the rotor damping, T_o is the mean torque applied to the rotor, and $T\sin(n\theta)$ is the fluctuating torque applied to the rotor.

Now, Lagrange's method can be applied to the kinetic energies and generalized forces to obtain the system's equations of motion. The rotor and absorbers equation of motion were respectively found to be:

$$\begin{aligned}&\left[J_r + mR^2 + m(L^2+\rho^2) + 2mRL\cos(\phi)\right]\ddot{\theta} + m(L^2+\rho^2+RL\cos(\phi))\ddot{\phi}\\ &- mRL\dot{\phi}\sin(\phi)\left[2\dot{\theta}+\dot{\phi}\right] - c_a\dot{\phi}\cos(\phi) - F_s\mathrm{sgn}(\dot{\phi})\cos(\phi) = T_o + T\sin(n\theta)\end{aligned} \tag{2.2}$$

$$m(L^2+\rho^2+RL\cos(\phi))\ddot{\theta} + m(L^2+\rho^2)\ddot{\phi} + mRL\dot{\theta}^2\sin(\phi) + c_a\dot{\phi} + F_s\mathrm{sgn}(\dot{\phi}) = 0 \tag{2.3}$$

The above equations of motion are non-linear with rotor to absorber coupling. The important quantity in Eqns.(2.2) and (2.3 is the rotor angular acceleration, $\ddot{\theta}$,

which is desired to be zero. If the angular acceleration of the rotor is zero, one can conclude the absorber has eliminated the rotor vibrations completely.

For the case in which the rotor is operating at a constant speed ($\dot{\theta} = \Omega$) and assuming small absorber angles, Eqn. (2.3) reduces to

$$m(L^2 + \rho^2)\ddot{\phi} + mRL\Omega^2\phi + c_a\dot{\phi} + F_s\text{sgn}(\dot{\phi}) = 0 \tag{2.4}$$

From Eqn. (2.4) it can easily be seen that the natural frequency of the absorber alone is given by

$$\omega_n = \Omega\sqrt{\frac{RL}{L^2 + \rho^2}}$$

which indicates the absorber's natural frequency is proportional to a given mean angular velocity. A common way to express this natural frequency is through a given order ($\tilde{n}$) multiplied by a mean angular velocity

$$\omega_n = \tilde{n}\Omega$$

where, in this case,

$$\tilde{n} = \sqrt{\frac{RL}{L^2 + \rho^2}}$$

2.2 Scaling and Non-Dimensionalizing of the Equations of Motion

The equations of motion developed in the previous section (Eqns. (2.2) and (2.3)) comprise an autonomous set of differential equations due to the fact that the cyclic applied torque, $T\sin(n\theta)$, is expressed as function of the rotor angle. To perform further analysis on these equations, using a scheme following that of Alsuwaiyan [1] and Nester [9], the independent variable is switched from time to the rotor angle. In order to accomplish this, a new non-dimensional variable is defined as

$$\nu = \frac{\dot{\theta}}{\Omega} \tag{2.5}$$

which is the ratio of the rotor's angular velocity to its mean velocity. This new variable will be used to express the rotor's speed and acceleration. Since our new independent variable is now θ, some relationships must be developed to relate time derivatives to those of θ. Using the chain rule, Alsuwaiyan [1] found these relationships to be

$$\begin{aligned} \dot{(*)} &= \frac{d(*)}{dt} = \Omega\nu\frac{d(*)}{d\theta} = \Omega\nu(*)' \\ \ddot{(*)} &= \frac{d^2(*)}{dt^2} = \Omega^2\nu\frac{d\nu}{d\theta}\frac{d(*)}{d\theta} + \Omega^2\nu^2\frac{d^2(*)}{d\theta^2} = \Omega^2\nu\nu'(*)' + \Omega^2\nu^2(*)'' \end{aligned} \tag{2.6}$$

i.e.

$$\ddot{\theta} = \frac{d^2\theta}{dt^2} = \Omega^2\nu\frac{d\nu}{d\theta} = \Omega^2\nu\nu'$$

Next, the absorber angle, ϕ, is converted to a non-dimensional arc length

$$s = \frac{L\phi}{\beta} \tag{2.7}$$

where β is a variable which will be used to make the equations readily comparable to the equations derived by Alsuwaiyan [1] for general path CPVA's. Substituting these new parameters into Equations (2.2) and (2.3), expanding the sines and cosines to

third order in s and rearranging gives

$$\begin{aligned}
&\left[1+\frac{m}{J}(L^2+R^2+\rho^2)+\frac{2mLR}{J}-\frac{mR\beta}{JL}s^2\right]\nu\nu' \\
&+\left[\epsilon-\frac{mR\beta^3}{2JL^2}s^2\right]\left[\nu\nu's'+\nu^2s''\right]-\frac{mR\beta^3}{JL^2}(\nu s')^2\left[s-\frac{\beta^2}{6L^2}s^3\right] \\
&-\frac{mR\beta^2}{JL}\nu^2 s'\left[2s-\frac{\beta^2}{3L^2}s^3\right]+\frac{\varphi(s^{prime})m\beta(L^2+\rho^2)}{JL}\left[\frac{\beta^2}{2L^2}-1\right] \\
&+\frac{\mu_a m(L^2+\rho^2)\beta}{JL}\nu s'\left[\frac{\beta^2}{2L^2}-1\right]+\mu_o\nu=\Gamma_o+\Gamma(\theta)
\end{aligned} \tag{2.8}$$

$$\begin{aligned}
&s'\nu'\nu+\nu^2s''+\frac{LR}{L^2+\rho^2}\left[s-\frac{\beta^2}{6L^2}s^3\right]\nu^2 \\
&\frac{L^2R}{\beta(L^2+\rho^2)}\left[-\frac{1}{2}\left(\frac{\beta s}{L}\right)^2+\frac{L^2+LR+\rho^2}{L}\right]\nu\nu'+\mu_a s'\nu+\varphi(s^{prime})=0
\end{aligned} \tag{2.9}$$

where

$$\begin{aligned}
\epsilon &= \frac{m\beta}{JL}(LR+L^2+\rho^2) \\
\mu_a &= \frac{c_a}{m\Omega(L^2+\rho^2)} \\
\varphi(s') &= \frac{F_s L}{m\beta\Omega^2(L^2+\rho^2)}\operatorname{sgn}\left(\frac{\nu\beta\Omega s'}{L}\right) \\
\mu_o &= \frac{c_o}{J\Omega} \\
\Gamma_o &= \frac{T_o}{J\Omega^2} \\
\Gamma(\theta) &= \frac{T\sin(n\theta)}{J\Omega^2}
\end{aligned} \tag{2.10}$$

The ϵ term defined above is physically the ratio of the pendulum's inertia to that of the rotor and will be used as the "small" parameter in the pertubation analysis later.

The task of relating Eqns. (2.8) and (2.9) to past forms will now be undertaken. Alsuwaiyan [1] and Chao [3] used the following non-dimensional equations of motion

for a rotor with a single, general path absorber:

$$\nu s'' + (s' + \tilde{g}(s))\nu' - \frac{1}{2}\frac{dx}{ds}(s)\nu + \mu_a s' = 0 \tag{2.11}$$

for the absorber and

$$\begin{aligned} &\frac{mR_o^2}{J}\left[\frac{dx}{ds}s'\nu^2 + x(s)\nu\nu' + \tilde{g}(s)s'\nu\nu' + \tilde{g}(s)s''\nu^2 + \frac{d\tilde{g}}{ds}(s)s^2\nu^2\right] + \nu\nu' \\ &= \frac{mR_o^2}{J}\mu_a\tilde{g}(s)s'\nu - \mu_o\nu + \Gamma_o + \Gamma(\theta) \end{aligned} \tag{2.12}$$

for the rotor equation. $x(s)$ in the above equations is a normalized function that describes the path followed by the absorber's center of mass. Referring to Figure 2.2, $x(s)$ is specifically the distance from 0 to c squared. Alsuwaiyan [1] showed the form of this function to be

$$x(s) = 1 - \tilde{n}^2 s^2 + \gamma s^4 + O(s^6) \tag{2.13}$$

in which

$$\gamma(s) = \left(\frac{1}{12}\right)(\tilde{n}^2 + 1)^2(\tilde{n}^2 - \lambda^2(\tilde{n}^2 + 1))$$

Denman [4] showed that λ can be used to describe curves that have very special properties; i.e. $\lambda = 1$ describes a cycloid, $0 < \lambda < 1$ describes certain epicycloids, and $\lambda = 0$ gives a circular path which will be used in this analysis.

The $\tilde{g}(s)$ term is also a path function that arises during the derivation of the general path CPVA equations of motion. Physically, $\tilde{g}(s)$ is the dot product of the unit vector in the θ direction and the unit vector in the direction of the absorber rotation, ϕ in this case. It is defined by

$$\tilde{g}(s) = \sqrt{x(s) - \frac{1}{4}\left(\frac{dx}{ds}(s)\right)^2} = 1 - \frac{1}{2}\tilde{n}^2(1 + \tilde{n}^2)s^2 + O(s^4) \tag{2.14}$$

If Eqn. (2.9) is divided through by ν and the ν' term is compared to that in Eqn.

(2.11) we get

$$\tilde{g}(s) = \frac{L^2 R}{\beta(L^2+\rho^2)}\left[-\frac{1}{2}\left(\frac{\beta s}{L}\right)^2 + \frac{L^2+LR+\rho^2}{L}\right] \tag{2.15}$$

Since it is desired to get the circular path absorber equations of motion in the same form as Eqns. (2.11) and (2.12), choosing

$$\beta = L\left(1+\tilde{n}^2\right) \tag{2.16}$$

forces $\tilde{g}(s)$ to take on the same form as Eqn. (2.14). Matching ν terms in Eqn. (2.9) to those in Eqn. (2.11) and recalling the definition of $\tilde{n}$ gives

$$\frac{dx}{ds} = -2\tilde{n}^2\left(s - \frac{\beta^2}{6L^2}s^3\right) \tag{2.17}$$

Integrating Eqn. (2.17) yields

$$x(s) = C - \tilde{n}^2 s^2 + \frac{\tilde{n}^2}{12}\left(1+\tilde{n}^2\right)s^4 \tag{2.18}$$

where C is the integration constant. Letting $C = 1$ the circular path absorber's path function becomes

$$x(s) = 1 - \tilde{n}^2 s^2 + \gamma_a s^4 \tag{2.19}$$

where

$$\gamma_a = \frac{\tilde{n}}{12}\left(\tilde{n}^2+1\right)^2$$

The circular path equations of motion are now conveniently scaled to match the same form used by past researchers and allows for comparison to their extensive work.

2.3 Averaged Equations for a Single Absorber

It has been shown by Alsuwaiyan [1] that by scaling terms in a certain way, one can uncouple the leading order rotor dynamics from those of the absorber. This scaling is

$$
\begin{aligned}
s &= \epsilon^{1/2} z \\
\mu_a &= \epsilon \tilde{\mu}_a \\
\varphi(s') &= \epsilon^{3/2} \tilde{\varphi}(s') \\
\mu_o &= \epsilon \tilde{\mu}_o \\
\Gamma_o &= \epsilon \tilde{\Gamma}_o \\
\Gamma(\theta) &= \epsilon^{3/2} \tilde{\Gamma}(\theta) \\
\nu &= 1 + \epsilon^{3/2} w \\
\tilde{n} &= n(1 + \epsilon\sigma)
\end{aligned}
\tag{2.20}
$$

where we have scaled the absorber amplitude, absorber viscous and Coulomb damping, rotor damping, mean torque, rotor oscillations and applied fluctuating torque. The order $\tilde{n}$ has also been scaled, where σ is the detuning parameter that allows for forcing the absorbers slightly away from their tuning order. Newland [10] showed that overtuning the pendulum allows for larger values of the cyclic torque amplitude to be applied before the dangerous "jump" in the pendulum's amplitude can occur. In this case, overtuning is defined as forcing at a lower order than the pendulum is tuned to ($n < \tilde{n}$). As will be shown experimentally and numerically this jump in absorber amplitude is accompanied by a 180° jump in phase. This causes the absorbers to amplify the torsional vibrations and must be avoided in practice.

Substituting the above scaled parameters into Eqns. (2.8) and (2.9), expanding and keeping terms to order $\epsilon^{3/2}$ gives the following equation for the absorber dynamics

$$z'' + n^2 z = \epsilon(2\gamma_o z^3 - 2n^2\sigma z - \tilde{\varphi}_a(s') - \tilde{\mu}_a z' - w') \tag{2.21}$$

where

$$\gamma_O = \frac{n^2}{12}(n^2+1)^2 \tag{2.22}$$

$$\tilde{\varphi}_a(s') = \frac{F_s}{m(1+n^2)\Omega^2(L^2+\rho^2)}\mathrm{sgn}\left(\frac{\nu\beta\Omega s'}{L}\right) \tag{2.23}$$

and

$$\epsilon(\tilde{\mu}_O - \tilde{\Gamma}_O) + \epsilon^{3/2}(w' + z'' - \tilde{\Gamma}(\theta)) = 0 \tag{2.24}$$

for the scaled rotor equation. It is noted that $\tilde{\Gamma}_O = \tilde{\mu}_O$ must hold to keep the rotor spinning at a constant mean speed. Inserting this balance into Eqn. (2.24) and solving for the rotor angular acceleration yields

$$w' = \tilde{\Gamma}(\theta) - z'' \tag{2.25}$$

which, with the known expression

$$z'' = \epsilon(f(z, z', \theta)) - n^2 z$$

where

$$\epsilon(f(z, z', \theta)) = \epsilon(2\gamma_O z^3 - 2n^2\sigma z - \tilde{\varphi}_a(s') - \tilde{\mu}_a z' - w')$$

conviently uncouples the absorber dynamics from those of the rotor. The final form for the weakly non-linear, weakly damped absorber equation is given by

$$z'' + n^2 z = \epsilon(2\gamma_O z^3 - 2n^2\sigma z - \tilde{\varphi}_a(s') - \tilde{\mu}_a z' - \tilde{\Gamma}(\theta) - n^2 z) \tag{2.26}$$

To solve for the non-dimensional rotor acceleration, Eqn. (2.21) can be used in Eqn. (2.25) to give

$$\nu\nu' = \epsilon^{3/2}\left(n^2 z + \tilde{\Gamma}(\theta)\right) \tag{2.27}$$

which is a good measure of the torsional vibrations the rotor is undergoing. One can solve for z from Eqn. (2.26), then can use that nonlinear result in Eqn. (2.27 to obtain the nonlinear rotor response.

To obtain approximate solutions to the equations of motion, the method of averaging is applied. To begin, we will express the absorber motion in polar coordinates that take the form

$$z = a\sin(n\theta + \alpha) \tag{2.28}$$

$$z' = na\cos(n\theta + \alpha) \tag{2.29}$$

where a is the amplitude of the steady-state absorber response and α is the corresponding phase. Both the amplitude and phase will, under our operating conditions, be slowly varying functions of the rotor angle, θ. Applying the method of averaging requires the constraint

$$a'\sin(n\theta + \alpha) + a\alpha'\cos(n\theta + \alpha) = 0 \tag{2.30}$$

to be made. Utilizing this coordinate transformation, the slowly varying amplitude and phase is found to be,

$$\begin{aligned} a' &= \cos(n\theta + \alpha)\frac{\epsilon}{n} f(a\sin(n\theta + \alpha), na\cos(n\theta + \alpha), \theta) \\ \alpha' &= -\sin(n\theta + \alpha)\frac{\epsilon}{na} f(a\sin(n\theta + \alpha), na\cos(n\theta + \alpha), \theta) \end{aligned} \tag{2.31}$$

where, for this case,

$$\epsilon f(a\sin(n\theta + \alpha), na\cos(n\theta + \alpha), \theta) = 2\gamma_O z^3 - 2n^2\sigma z - \tilde{\varphi}_a - \tilde{\mu}_a z' - \tilde{\Gamma}(\theta) - n^2 z$$

The "small" function, ϵf, is periodic in θ with a period of $\frac{2\pi}{n}$. Averaging the above

equations over a single period yields

$$\bar{a}' = \epsilon \left(-\frac{\tilde{\mu}_a}{2}\bar{a} - \frac{2\tilde{\varphi}_b}{\pi} + \frac{\tilde{\Gamma}(\theta)}{2n} \sin\bar{\alpha} \right) \tag{2.32}$$

$$\bar{a}\bar{\alpha}' = \epsilon \left(-\frac{3\gamma_o}{4n}\bar{a}^3 + n\bar{a}(\sigma + \frac{1}{2}) + \frac{\tilde{\Gamma}(\theta)}{2n} \cos\bar{\alpha} \right) \tag{2.33}$$

where

$$\tilde{\varphi}_b = \frac{F_s}{m(1+n^2)\Omega^2(L^2+\rho^2)}$$

In order to solve for the the steady state amplitude and phase, we set $\bar{a} = a_{ss}$ =constant and $\bar{\alpha} = \alpha_{ss}$ =constant to get

$$\frac{\tilde{\Gamma}}{2n}\sin(\alpha_{ss}) = \frac{\tilde{\mu}_a}{2}a_{ss} + \frac{2\tilde{\varphi}_b}{\pi} \tag{2.34}$$

$$\frac{\tilde{\Gamma}}{2n}\cos(\alpha_{ss}) = \frac{3\gamma_o}{4n}a_{ss}^3 - na_{ss}(\sigma + \frac{1}{2}) \tag{2.35}$$

Using $\cos^2 x + \sin^2 x = 1$, the steady state phase can be eliminated from Eqns. (2.34) and (2.35) and the amplitude of fluctuating torque can be solved for in terms of the steady-state absorber amplitude:

$$\tilde{\Gamma} = \sqrt{\left(\frac{\tilde{\mu}_a}{2}a_{ss} + \frac{2\tilde{\varphi}_b}{\pi}\right)^2 + \left(\frac{3\gamma_o}{4n}a_{ss}^3 - na_{ss}(\sigma + \frac{1}{2})\right)^2} \tag{2.36}$$

The above equation is similar to that of Nester [9], with the exception of the $\tilde{\varphi}_b$ term, which represents the Coulomb friction. Equation 2.36 can be used to evaluate the absorber's steady-state amplitude as a function of the applied torque on the rotor. Using Eqn. (2.36) the amplitude of the non-dimensional fluctuating torque, $\tilde{\Gamma}$, that it takes the overcome the dry friction and produce an absorber oscillation can be easily

solved for. Letting $a_{SS} = 0$ one can find

$$\tilde{\Gamma} > \frac{2\tilde{\varphi}_b}{\pi} \tag{2.37}$$

to obtain any absorber response.

With Eqns. (2.27) and (2.36) some initial investigations can be performed on the effects of Coulomb friction in the performance of the absorber. Figure 2.3 shows the non-dimensional absorber amplitude as a function of the non-dimensional fluctuating torque for the case of an equivalent viscous damping model used by past researchers as well as a Coulomb and viscous damping model. It should be noted that the values used for the damping parameters are the ones which are estimated in the following chapter, so the trend of the plots does correspond to that of the experimental rig (see Table 3.2 for values).

From Figure 2.3 it is evident that as the amplitude of applied torque increases, the absorbers go unstable (indicated by the dotted lines) and the "jump" phenomenon occurs. This "jump" is accompanied by a 180° shift in the phase between the absorber and the rotor. This phase shift of the absorber results in an increase in the torsional vibrations on the rotor. This is observed by plotting the rotor angular acceleration amplitude against the applied fluctuating torque amplitude as shown in Figure 2.4.

Looking at Figures 2.3 and 2.4 it can easily be seen that the Coulomb term allows for a greater torque to be applied to the rotor before the absorber goes unstable. It is also noted that because of the friction, the absorber "sticks" for a range of small torques and the rotor's angular acceleration is as if the absorber is locked. As the level of Coulomb friction is increased, one would expect it would take a greater level of fluctuating torque to achieve some absorber oscillation. To confirm this, Figure 2.5 displays the steady-state amplitude of absorber oscillations versus the amplitude of fluctuating torque for different levels of Coulomb friction. It is evident that as the level

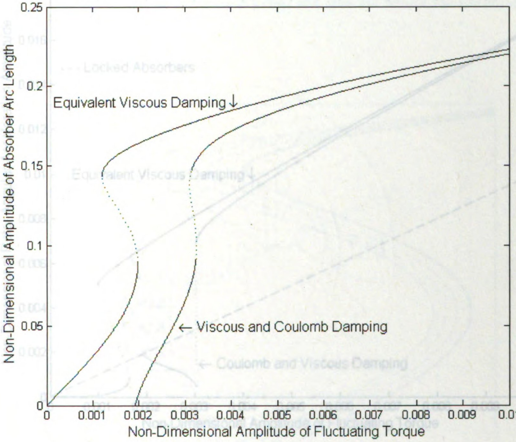

Figure 2.3: Non-Dimensional Absorber Amplitude vs. Non-Dimensional Fluctuating Torque Amplitude for the Different Damping Models and $\sigma = 0$. (a_{SS} vs. Γ)

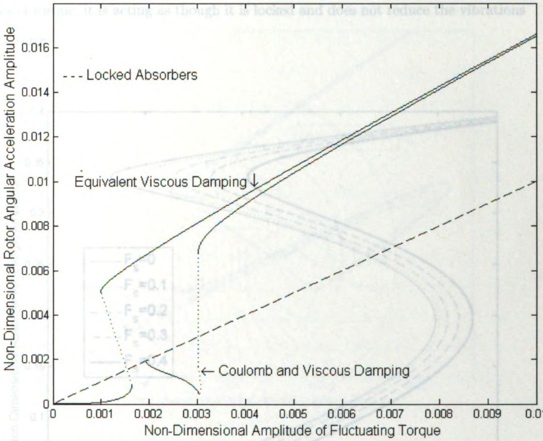

Figure 2.4: Non-Dimensional Rotor Acceleration Amplitude vs. Non-Dimensional Fluctuating Torque Amplitude for the Different Damping Models and $\sigma = 0$. ($\nu\nu'$ vs. Γ)

of Coulomb friction is increased, the absorber sticks for a larger level of fluctuating torque and also becomes unstable at a larger torque level. The effectiveness of the absorber as the Coulomb friction is increased can be investigated by plotting the angular acceleration of the rotor against the amplitude of the fluctuating torque. This is shown in Figure 2.6 and one can notice that as the absorber sticks for larger values of torque, it is acting as though it is locked and does not reduce the vibrations of the rot0r.

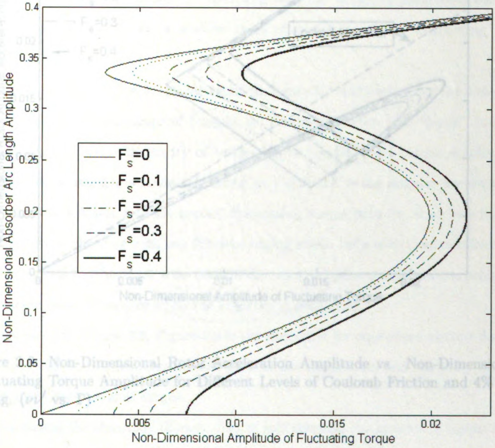

Figure 2.5: Non-Dimensional Absorber Amplitude vs. Fluctuating Torque Amplitude for Different Levels of Coulomb Friction and 4% detuning. (a_{SS} vs. Γ)

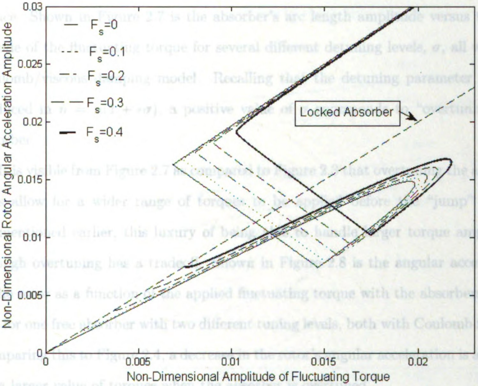

Figure 2.6: Non-Dimensional Rotor Acceleration Amplitude vs. Non-Dimensional Fluctuating Torque Amplitude for Different Levels of Coulomb Friction and 4% detuning. ($\nu\nu'$ vs. Γ)

As will be shown, the common approach to avoiding these dangerous "jumps" is to overtune the absorber to allow for a greater range of torque to be applied. With overtuning comes a decrease in performance of the absorbers. Therefore, successfully estimating the correct damping model in this case will allow for a lower detuning level to avoid the instabilities.

We now to turn to the effect that detuning the absorbers has on their performance. Shown in Figure 2.7 is the absorber's arc length amplitude versus the amplitude of the fluctuating torque for several different detuning levels, σ, all with the Coulomb/viscous damping model. Recalling that the detuning parameter was introduced in $\tilde{n} = n(1 + \epsilon\sigma)$, a positive value of σ coorsponds to "overtuning" the absorber.

It is visible from Figure 2.7 as compared to Figure 2.3 that overtuning the absorber does allow for a wider range of torques to be applied before the "jump" occurs. As mentioned earlier, this luxury of being able to handle larger torque amplitudes through overtuning has a tradeoff. Shown in Figure 2.8 is the angular acceleration of the rotor as a function of the applied fluctuating torque with the absorbers locked and for one free absorber with two different tuning levels, both with Coulomb friction. Comparing this to Figure 2.4, a decrease in the rotor's angular acceleration is achieved for a larger value of torques when the absorber is overtuned.

Compared to Figure 2.8, Figure 2.9 is the same plot for equivalent viscous damping. As is visible, the absorber doesn't stick at low amplitudes and the jump occurs at a slightly lower level of torque.

Overtuning the absorbers though, does in fact decrease the amount of torque that is absorbed as is visible from Figures 2.7 and 2.8. Choosing the correct detuning to avoid the dangerous jumps while still obtaining a desired reduction in torsional vibrations is a design problem that is application specific.

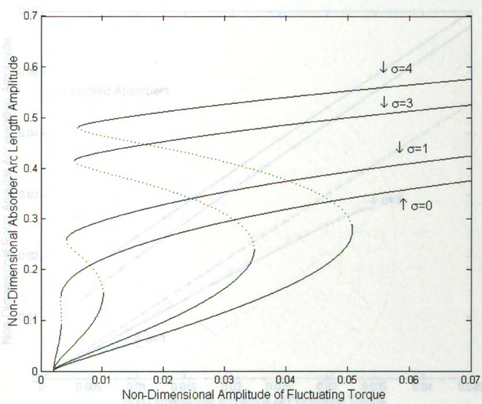

Figure 2.7: Absorber Amplitude vs. Fluctuating Torque Amplitude for Different Detuning Values. (a_{SS} vs. Γ)

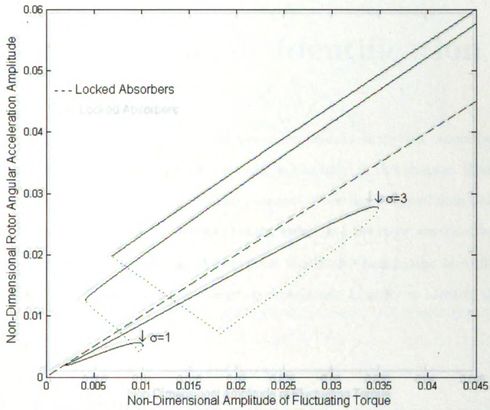

Figure 2.8: Rotor Angular Acceleration vs. Fluctuating Torque Amplitude for Different Detuning Values using a Viscous/Coulomb Damping Model. ($\nu\nu'$ vs. Γ)

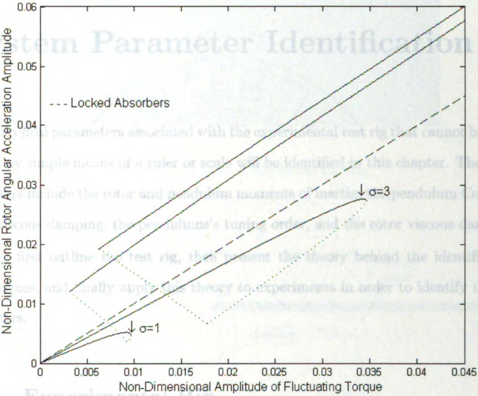

Figure 2.9: Rotor Angular Acceleration vs. Fluctuating Torque Amplitude for Different Detuning Values using an Equivalent Viscous Damping. ($\nu\nu'$ vs. Γ)

Chapter 3

System Parameter Identification

The physical parameters associated with the experimental test rig that cannot be measured by simple means of a ruler or scale will be identified in this chapter. These parameters include the rotor and pendulum moments of inertia, the pendulum Coulomb and viscous damping, the pendulums's tuning order, and the rotor viscous damping.

We first outline the test rig, then present the theory behind the identification techniques, and finally apply this theory to experiments in order to identify the parameters.

3.1 Experimental Rig

A photo of the experimental rig is shown in Figure 3.1 followed by a schematic in Figure 3.2.

The rotor is equipped with two absorbers that can be locked or free, as well as two "weights" that increase the inertia of the rotor (decrease ϵ). The angle of the free absorber is measured via an optical encoder. The rotor speed is also measured by an optical encoder that allows for measurement of the shaft's mean speed as well as its oscillations about that mean speed. The torque being supplied to the rotor is

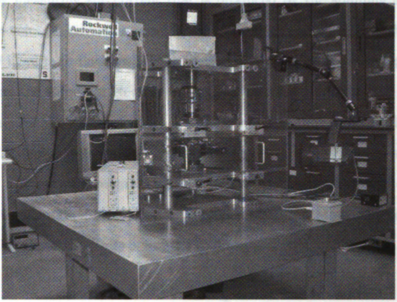

Figure 3.1: Photo of Experimental Rig.

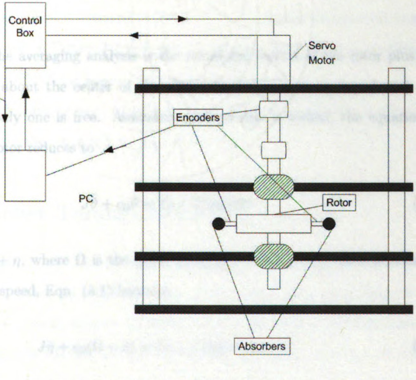

Figure 3.2: Schematic of Experimental Rig.

quantified by measuring the current that is produced by the spinning of the rotor. A current to voltage conversion is set in the control box which allows the torque to be displayed in volts in Labview. Using inertial properties of the motor given by the manufacturer, the torque in Newton-meters can then be obtained from the voltage measurement. All three of these signals (absorber angle, rotor speed, and torque) are fed into a PC running Labview which allows for real-time viewing and post processing of the data. The Labview program also allows for PID feedback control of the mean rotor speed to maintain a nearly constant mean speed. The error analysis associated with all of these measurements is located in Appendix A. [1]

3.2 Rotor and Absorber Inertia

The J used in the averaging analysis is the rotational inertia of the rotor plus one locked absorber about the center of the rotor, since our rig is equipped with two absorbers, but only one is free. Assuming the absorber is locked, the equation of motion for the rotor reduces to

$$J\ddot{\theta} + c_O\dot{\theta} = T_O + T\sin(n\theta) \tag{3.1}$$

Letting $\theta = \Omega t + \eta$, where Ω is the mean rotor speed and η is a small fluctuation about the mean speed, Eqn. (3.1) becomes

$$J\ddot{\eta} + c_O(\Omega + \dot{\eta}) = T_O + T\sin(n(\Omega t + \eta)) \tag{3.2}$$

[1]Thanks to Ryan Monroe for doing most of the work on this

Noting that the rotor damping must equal the mean torque for the rotor to spin at a constant mean speed ($c_O\Omega = T_O$), Eqn. (3.1) reduces to

$$J\ddot{\eta} + c_O\dot{\eta} = T\sin(n(\Omega t + \eta)) \tag{3.3}$$

Neglecting the $c_O\dot{\eta}$ term, as it can be assumed to be very small, one obtains:

$$J\ddot{\eta} = T\sin(n(\Omega t + \eta)) \tag{3.4}$$

Equation 3.3 shows that if we experimentally sweep through a range of forcing amplitudes, T, measure the rotor acceleration, $\ddot{\theta}$, at each T and plot the angular acceleration as a function of the applied torque the result should be a line with a slope of $1/J$. As mentioned in the previous section, T is measured from the motor current but one can only measure $\dot{\theta}$ from the shaft encoder. To obtain $\ddot{\theta}$, the signal from the shaft encoder can be multiplied by the shaft's frequency, $n\Omega$, to calculate the rotor angular acceleration. Shown in Figure 3.3 is a plot of the experimental rotor acceleration against the magnitude of the applied fluctuating torque.

The data is obviously linear, therefore fitting a line to the data can reveal the rotational inertia of the rotor and one locked absorber.

3.3 Absorber Tuning Order and Inertia

Using purely linear theory, Den Hartog [5] showed that a perfectly tuned absorber, $n = \tilde{n}$, with zero damping and modeled as a point mass on a rotor behaves like a system with an infinite amount of inertia as it completely eliminates torsional vibrations. From this, as well as the information in Figure 2.8 which shows the highest decrease in torsional vibrations at the tuning order, one can conclude that for a constant amplitude of fluctuating torque, the angular acceleration of the rotor

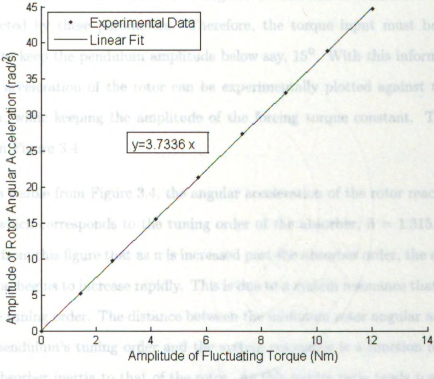

Figure 3.3: Angular Acceleration Amplitude of the Rotor vs. the Amplitude of Fluctuating Torque Applied.

is at its minimum precisely when the absorber is perfectly tuned. We must be careful though, as the pendulum can swing at large amplitudes, rendering, by nonlinearity, the frequency as a function of the pendulum amplitude. For example, the non-linear effects of a large torque input and corresponding large absorber oscillations will shift the effective tuning order to a value which is smaller than the actual $\tilde{n}$. Recall the formula for $\tilde{n}$ consists of purely geometric parameters, but the non-linear effects can cause one to observe a minimum rotor angular acceleration at a different value which is predicted by these parameters. Therefore, the torque input must be kept low enough to keep the pendulum amplitude below say, 15°. With this information, the angular acceleration of the rotor can be experimentally plotted against the forcing order, n, while keeping the amplitude of the forcing torque constant. This plot is shown in Figure 3.4.

As is visible from Figure 3.4, the angular acceleration of the rotor reaches a minimum, which corresponds to the tuning order of the absorber, $\tilde{n} = 1.315$. It is also evident from this figure that as n is increased past the absorber order, the angular acceleration begins to increase rapidly. This is due to a system resonance that is located past the tuning order. The distance between the minimum rotor angular acceleration at the pendulum's tuning order and the system resonance is a function of the ratio of the absorber inertia to that of the rotor. As this inertia ratio tends toward 0, the minimum of rotor angular acceleration and the system resonance fall exactly at the same order. Intuitively, this makes sense as a very small absorber and huge rotor ($\epsilon \approx 0$), will essentially be a single degree-of-freedom system with the absorber not having any effect on the rotor dynamics.

With the absorber tuning order known, the absorber's radius of gyration, ρ, can be easily determined from

$$\tilde{n} = \sqrt{\frac{RL}{L^2 + \rho^2}},$$

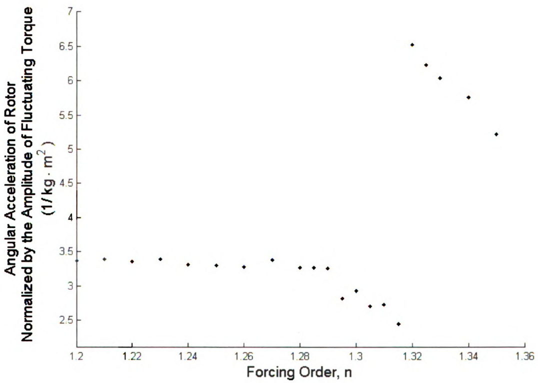

Figure 3.4: Normalized Rotor Angular Acceleration vs. Forcing Order, n.

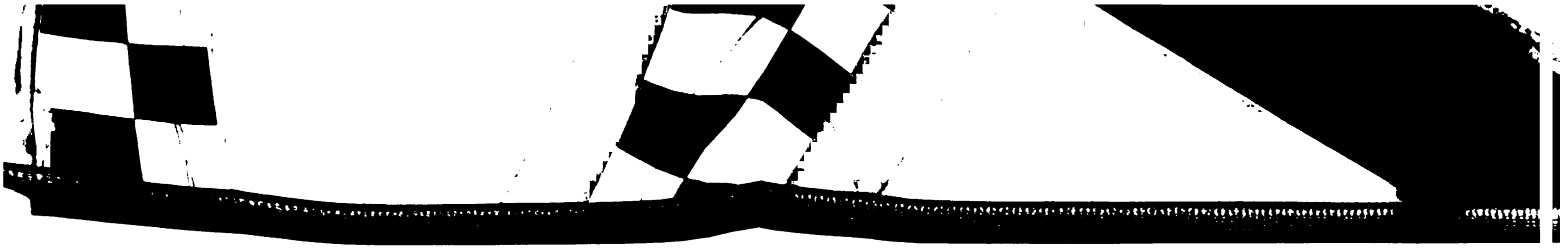

where R and L are easily measured from the system.

3.4 Determination of Absorber Damping

We model the damping in the absorber as viscous and Coulomb. Following a scheme by Liang and Feeny [7], these damping parameters can be successfully determined from free vibration information. Past researchers used an equivalent viscous model, and the problems with this will be shown.

First, the simultaneous viscous/Coulomb decrement method is outlined and then improved upon to account for noise and low resolution in the experimental data. The estimated parameters are then simulated and plotted against the experimental free vibration decay. The equivalent viscous model is also introduced and plotted to show the effects of the dry friction. It should also be noted that the method used to identify the damping parameters assumes not only a linear stiffness but also a single degree-of-freedom (DOF) free vibration. More specifically Eqn. (2.4) will be used to model the absorber in this case. To deal with the linear stiffness assumption, an experimental free vibration is conducted for a maximum absorber angle of 16°. In this range the assumption of $\sin\phi \approx \phi$ and $\cos\phi \approx 1$ is assumed to be valid. With respect to the single DOF assumption, the system being investigated consists of a pendulum coupled to a rotor and it technically consists of two DOF. The ratio of the inertia of the pendulum to that of the rotor is very small in this case, and it is this parameter which allows one to apply to single DOF method with a large value of accuracy. With a small inertia ratio, the coupling between the absorber and rotor is very weak.

where R and L are easily [illegible]

3.4 Determination of [illegible] Damping

We model the damping [illegible] Coulomb. Following a scheme by Liang and Feeny [illegible] can be successfully determined from free vibration [illegible] compared to equivalent viscous models, and the problems [illegible].

First, the simultaneous [illegible] method is outlined and then improved upon to [illegible] low resolution in the experimental data. The estimated parameters [illegible] tabulated and plotted against the experimental free vibration decay. The equivalent viscous model is also introduced and plotted to show the effects of the dry friction. It should also be noted that the method used to identify the damping parameters assumes not only a linear stiffness but also a single degree-of-freedom (DOF) free vibration. More specifically Eqn. (2.4) will be used to model the absorber in this case. To deal with the linear stiffness assumption, an experimental free vibration is conducted for a maximum absorber angle of 10°. In this range the assumption of $\sin\phi \approx \phi$ and $\cos\phi \approx 1$ is assumed to be valid. With respect to the single DOF assumption, the system being investigated consists of a pendulum coupled to a rotor and it technically consists of two DOF. The ratio of the inertia of the pendulum to that of the rotor is very small in this case, and it is this parameter which allows one to apply to single DOF method with a large value of accuracy. With a small inertia ratio, the coupling between the absorber and rotor is very weak.

3.4.1 Simultaneous Viscous/Coulomb Decrement Method

Lets consider a single DOF translational oscillator with viscous and Coulomb damping undergoing free vibration:

$$m\ddot{x} + c\dot{x} + kx + F_k \mathrm{sgn}(\dot{x}) = 0 \tag{3.5}$$

Referring to Eqn. (2.4), it is quite obvious that, for our case:

$$\begin{aligned} x &= \phi \\ m &= m(L^2 + \rho^2) \\ k &= mRL\Omega^2 \\ c &= c_a \\ F_s &= F_s \end{aligned} \tag{3.6}$$

Rearranging Eqn. (3.5) into standard oscillator form and setting conditions on $\dot{x}$ to eliminate the sgn we get

$$\ddot{x} + 2\zeta\omega_n\dot{x} + \omega_n^2 x = -\omega_n^2 x_k \qquad \dot{x} > 0 \tag{3.7}$$

and

$$\ddot{x} + 2\zeta\omega_n\dot{x} + \omega_n^2 x = +\omega_n^2 x_k \qquad \dot{x} < 0 \tag{3.8}$$

where $x_k = F_k/k$. Using this, we can solve (3.5) for every half cycle and find the amplitude of response noting that $\dot{x} = 0$ when direction is changed. Let's begin with $x(t_0) = X_o > 0$ and $\dot{x}(t_0) = 0$. With these initial conditions we know the motion will begin with a negative $\dot{x}$, i.e we can solve (3.8) for $x(t)$ to get

$$x(t) = (X_o - x_k)e^{-\zeta\omega_n(t-t_0)}\cos(\omega_d(t-t_0)) + \beta\sin(\omega_d(t-t_0)) + x_k \tag{3.9}$$

where $\beta = \zeta/\sqrt{1-\zeta^2}$ and $\omega_d = \omega_n\sqrt{1-\zeta^2}$. This solution for $x(t)$ will hold until the motion reaches its negative peak ($\dot{x} = 0$) which will be a half period ($t = t_1 = t_0 + \pi/\omega_d$) later in time. Using these conditions, the extreme displacement at this point can be found to be

$$X_1 = x(t_1) = -e^{-\beta\pi}X_0 + (e^{-\beta\pi} + 1)x_k \tag{3.10}$$

Assuming that the mass doesn't stick, then the mass will now reverse its motion and continue with $\dot{x} > 0$. Therefore (3.7) can be solved, and using similar conditions ($\dot{x} = 0$ and $t = t_2 = t_1 + \pi/\omega_d$) as before the extremum when the mass reaches this positive peak will be

$$X_2 = x(t_2) = -e^{-\beta\pi}X_1 - (e^{-\beta\pi} + 1)x_k \tag{3.11}$$

Continuing this process of solving for the extrema at each half cycle leads to a recursive relationship for X (the successive maximums and minimums of the response),

$$X_i = -e^{-\beta\pi}X_{i-1} + (-1)^{i-1}(e^{-\beta\pi} + 1)x_k, \qquad i = 1, 2, ..., n \tag{3.12}$$

Which is valid until the mass sticks. The stick criterion is $absX_i \leq F_s/k$, where F_s is the static friction. To isolate the viscous effect we can sum successive expressions for $X_i's$. To show this let's find X_{i+1} as

$$X_{i+1} = -e^{-\beta\pi}X_i + (-1)^i(e^{-\beta\pi} + 1)x_k \tag{3.13}$$

It can easily be seen that $(-1)^{i-1}$ and $(-1)^i$ have opposite signs, so adding (3.12)

with (3.13) and rearranging gives

$$\frac{X_i + X_{i+1}}{X_{i-1} + X_i} = -e^{-\beta\pi} \tag{3.14}$$

And we can solve for β. Once β is found, x_k can be solved for using (3.12).

3.4.2 Modifying the Method for Dealing with Noise and Low Resolution in Experiments

The formulas for finding β (3.14) and then x_k (3.12) use 3 consecutive measurements of the peak amplitudes of response. Thus, if there is noise and/or a low resolution displacement device is used, the method breaks down. To deal with this, we can generalize (3.12) to allow a range of $i + m$ half cycles to i half cycles (done by expanding out Eqn. (3.12) and substituting in the expression for X_{i-1}), such that

$$X_{i+m} = (-1)^m e^{-m\beta\pi} X_i + (-1)^{i+m-1}(e^{-\beta\pi} + 1)x_k \sum_{j=1}^{m} e^{-(m-j)\beta\pi} \tag{3.15}$$

This allows for a measurement over a range of m half cycles. I.e

$$\frac{X_m + X_{i+m}}{X_{i-1} + X_i} = -e^{-m\beta\pi} \tag{3.16}$$

But, we can even do better! If we let $i \to i + n$ then the measurement of consecutive half-cycles can be avoided all together. Doing this we obtain

$$\frac{X_{i+m} - X_{m+n+i}}{X_i - X_{i+n}} = (-1)^m e^{-m\beta\pi} \qquad n \text{ even} \tag{3.17}$$

and

$$\frac{X_{i+m} + X_{m+n+i}}{X_i + X_{i+n}} = (-1)^m e^{-m\beta\pi} \qquad n \text{ odd} \tag{3.18}$$

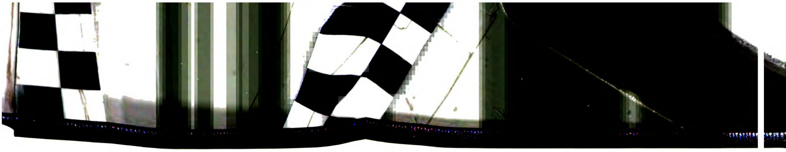

The numerator and denominator mark the difference in extrema over n half cycles. The ratio expresses how these differences are changing over a decay of n half cycles. Therefore, β can be estimated from either (3.17) or (3.18), then x_k can be found from (3.15). If $m = n$ then we need only 3 measurements, which can be taken to cover the entire span of decaying oscillation. Shown in Figure 3.5 is how using n and m, more cycles of decay are averaged as well as larger differences between the cycles. Both these help improve the accuracy of the decrement scheme.

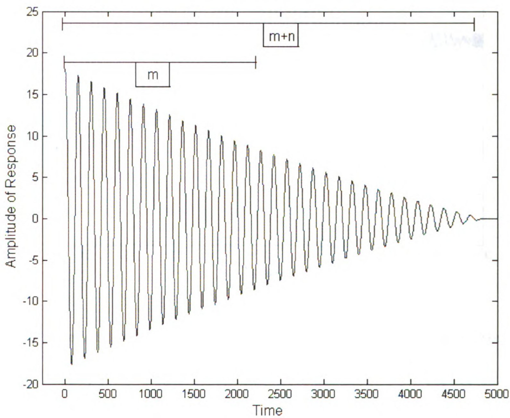

Figure 3.5: Qualitative Visualization of the Effect the Indices m and n have on the Method.

To test the efficacy of the improved decrement method, simulations were conducted on a linear, single DOF oscillator with viscous and Coulomb damping under-

going free vibration. Gaussian white noise was embedded into the response signal at a signal to noise power ratio of 20 decibels. This signal is shown in Figure 3.6, and the effect of adding noise is clearly evident.

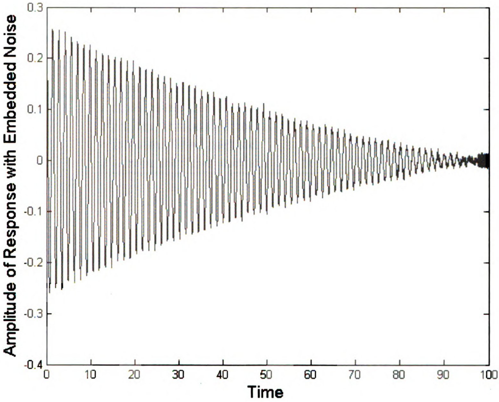

Figure 3.6: Free Vibration of Simulated Oscillator Response with Embedded Noise.

The unmodified decrement scheme was first applied to the decay and the identified damping coefficients were compared to the actual coefficients used in the simulation. Next, the improved method was used to identify the damping parameters from the noisy signal. Shown in Table 3.1 are the results, the parameter c is the viscous damping coefficient and F_S is the Coulomb term ($c = 0.2$ and $F_S = 0.11$ were the values used in the simulations). Looking at Table 3.1, it is obvious that the unmodified method breaks down severely in the presence of noise. The modified method identifies

the parameter with less than 8% error. This suggests that the method is robust, even in the presence of strong noise, and when applying this method to experimental data one would expect even a lower error in the estimated parameters as the noise in the experimental data is much smaller than what was simulated.

Table 3.1: Estimated Parameters Using the Original Decrement Method and Using the Modified Method .

Parameter Estimated	Value	Error
c from unmodified method	-15.3	7750%
F_S from unmodified method	7.72	6918%
c from modified method	0.184	8%
F_S from modified method	0.116	5.45%

3.4.3 Equivalent Viscous Model

The equivalent viscous model used by past researchers assumes purely viscous damping in the absorber. It can easily be shown by solving a linear oscillator equation with "small" viscous damping that the ratio of two successive peaks is

$$\ln\left(\frac{X_1}{X_2}\right) \cong 2\pi\zeta$$

where ζ is the damping ratio. To improve the accuracy of this, more than two peaks of the oscillation can be spanned such that

$$\ln\left(\frac{X_1}{X_{1+i}}\right) \cong 2i\pi\zeta$$

which implies that plotting $\ln\left(\frac{X_1}{X_{1+i}}\right)$ versus i should yield a line with a slope of $2\pi\zeta$ if the damping is indeed viscous.

A plot of $\ln\left(\frac{X_1}{X_{1+i}}\right)$ vs. i is shown in Figure 3.7 for a small amplitude ($\phi \approx 16^\circ$)

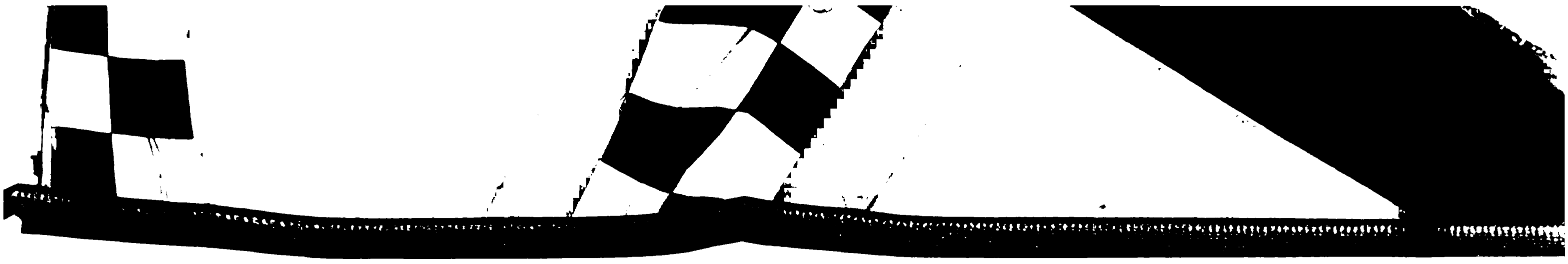

decay. The same plot is shown for a larger amplitude ($\phi \approx 37^{\circ}$) decay in Figure 3.8. It is obvious from both plots (especially the larger amplitude decay) that a completely viscous damping model does not fit the data well. If the damping was indeed only viscous, the data should be linear throughout the entire range of oscillations. In the plots, as i increases (physically meaning the amplitude is getting smaller), the data radically deviates from linearity and appears to grow exponentially. This is promising, as Coulomb friction, if present, dominates at smaller amplitudes and not accounting for this could be the cause for the deviation from linearity at low amplitudes.

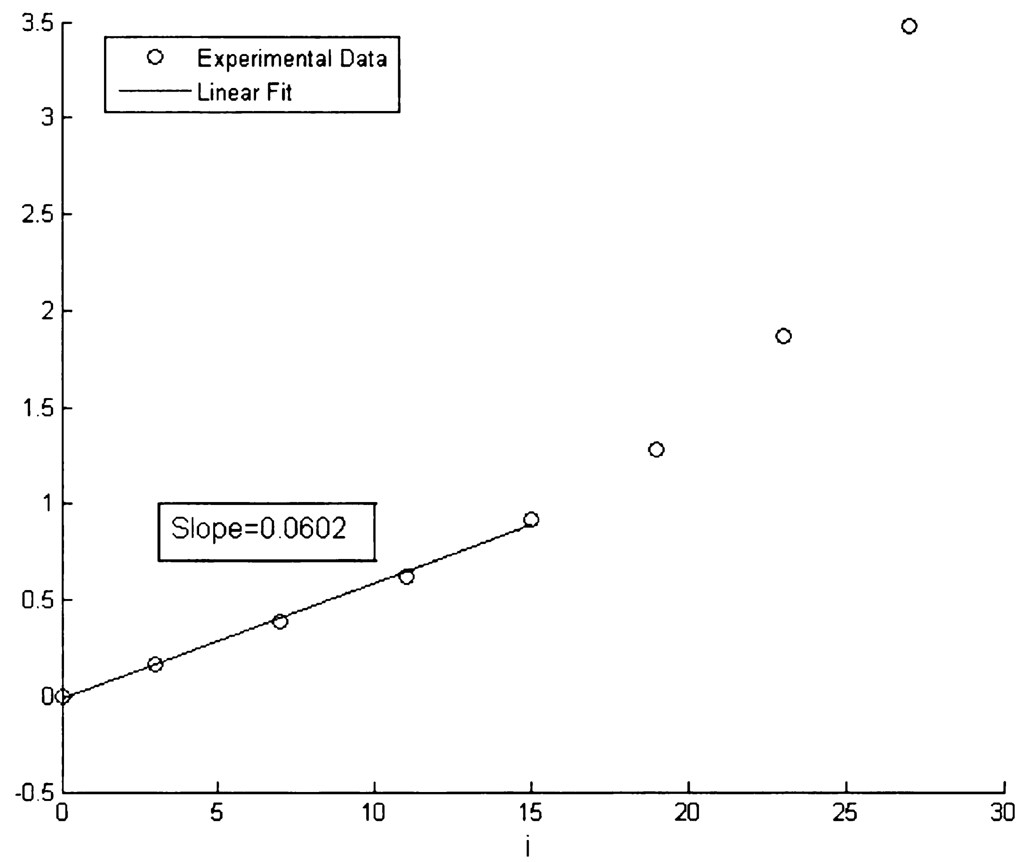

Figure 3.7: Small Amplitude Logarithmic Decrement.

Assuming that viscous damping dominates at larger amplitudes, the large am-

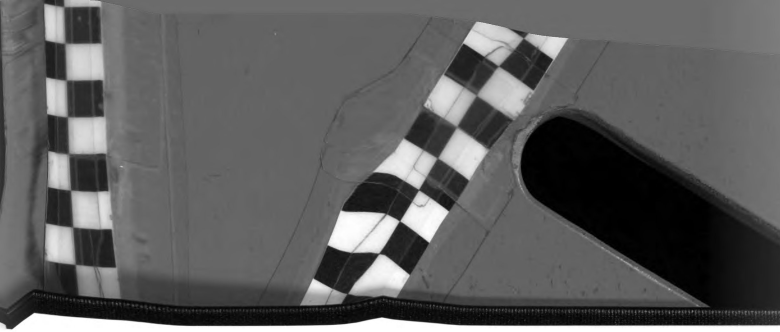

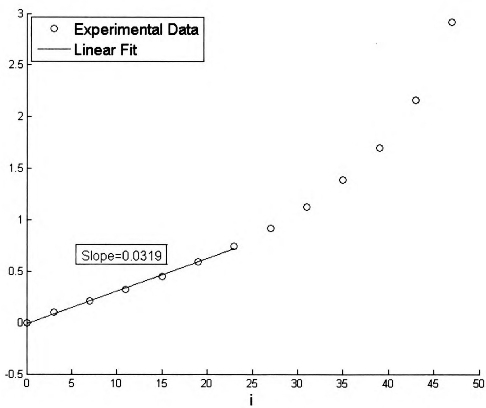

Figure 3.8: Large Amplitude Logarithmic Decrement.

plitude equivalent viscous parameter will be used for comparison to the viscous and Coulomb models in a later chapter.

3.4.4 Results

To get average β and x_k values from free vibration data for a circular path absorber, we chose an $m + n$ that covered the entire range of free oscillations with m and n directly in the middle of the response. These β and x_k values were then simulated in a free vibration response and compared to the experimental data. It should be noted that the viscous and Coulomb parameters are estimated assuming a linear stiffness, which is true of the absorber for small angles. Thus, an experimental free vibration was conducted from a maximum amplitude of 16°. The simulations used to compare the identified damping parameters against the experimental results are the fully non-linear, coupled equations. Simulating the coupled, non-linear equations allows for confirmation of the earlier assumptions (linear-stiffness, effective single DOF). This is shown in Fig. 3.9.

It is visible from Figure 3.9 that the parameters extracted from the simultaneous viscous/Coulomb method track the experimental data very closely. The low amplitude equivalent viscous damping model predicts much more damping than seems to be present. To quantify how good this data fits the model we can look at the residuals. To define our residual, let the amplitude of response that our estimated damping coefficients predicted be defined as $\tilde{X}_i$ and the experimental amplitude be X_i. The residual is then defined by

$$r = \frac{\tilde{X}_i - X_i}{|X_i|} \tag{3.19}$$

which is a normalized quantity. To get around resolution issues once again, we computed this residual for every 4 half periods. Shown in Figure 3.10 is graph of this data for the Coulomb plus viscous model.

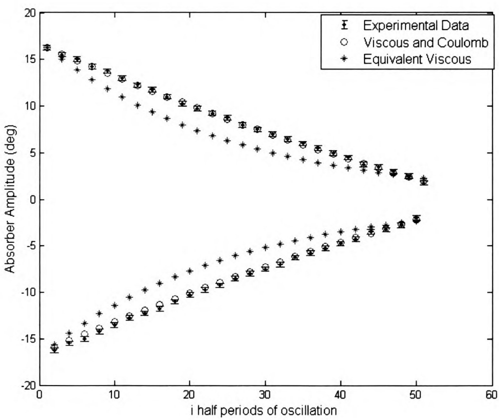

Figure 3.9: Theoretical vs. Experimental Free Vibration Peak Values for Small Amplitudes.

Figure 3.9: Theoretical vs. Experimental Free Vibration Peak Values for Small Amplitudes.

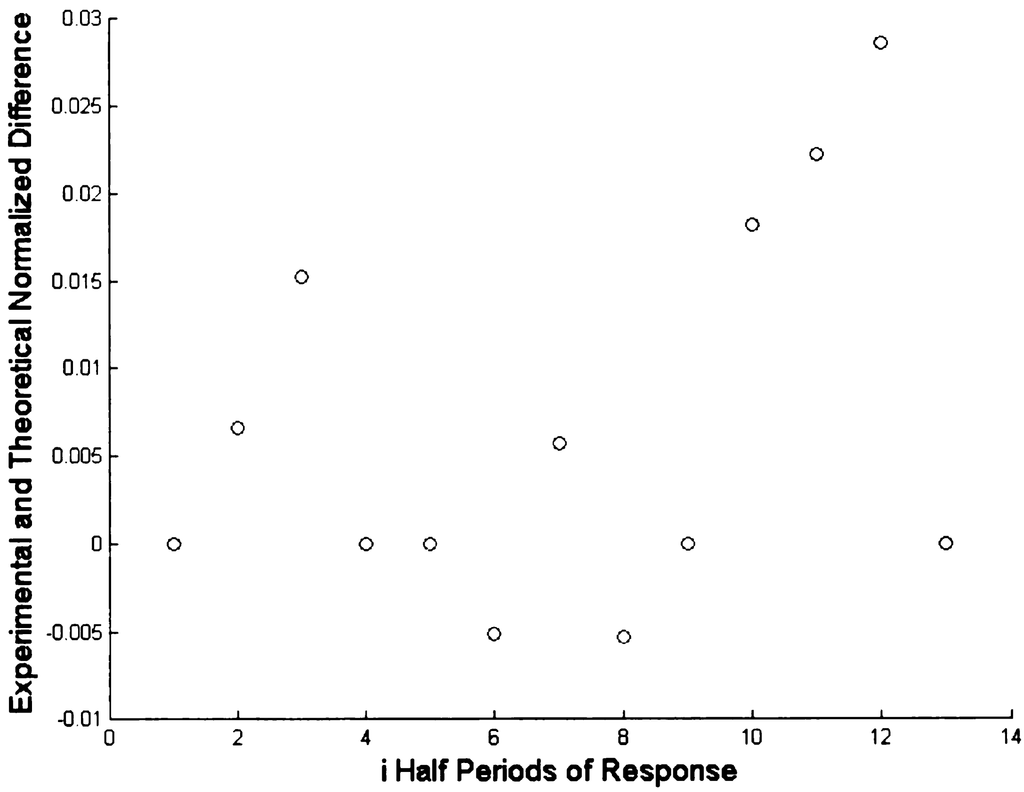

Figure 3.10: Residuals of the Damping Estimation.

From Figure 3.10, the residuals seem to exhibit a random behavior, oscillating with small amplitudes about 0. In a statistical sense, this is ideal; if the residuals exhibit some sort of pattern it could be concluded that the model is incorrect [2].

Next, the identification scheme was applied to a large amplitude (37°) decay. Recalling that the parameters were extracted assuming a linear stiffness, the pendulum's frequency decreases with increasing amplitude, and recalling $\zeta = \frac{c}{2m\omega_n}$, one would expect that the viscous damping would increase at larger amplitudes. Noting that the viscous damping should dominate at larger amplitudes, the total damping of the system should increase. It is found that the viscous damping term is smaller for the large amplitude free vibration and the Coulomb term is larger than the small amplitude decay (see Table 3.2). Figure 3.11 shows simulations of the fully non-linear, coupled equations using the damping parameters extracted from the large amplitude ring-down plotted against the experimental results. Also shown is the equivalent viscous response from the viscous parameter calculated in Figure 3.8.

The theory again seems to track the experiments quite well. As mentioned earlier, the value of the viscous damping was expected to be greater for the large amplitude decay and turned out to be smaller. Some reasons for this could be that the damping is a function of the amplitude, the bearing in the absorber could have heated up, thus causing a decrease in the viscous damping, or there could be another, possibly non-linear damping parameter present in the absorber.

To further examine this, the damping parameters extracted from the small amplitude decay were simulated in a large amplitude free vibration (37°) and compared to the large amplitude experimental data. It should be expected, knowing the large amplitude damping parameter, that the simulated response should be smaller in amplitude (due to the larger viscous term) for large amplitudes and then approach and track the experimental results nicely for amplitudes of response similar to those in Figure 3.9. Figure 3.12 displays the experimental results for a large amplitude ring-

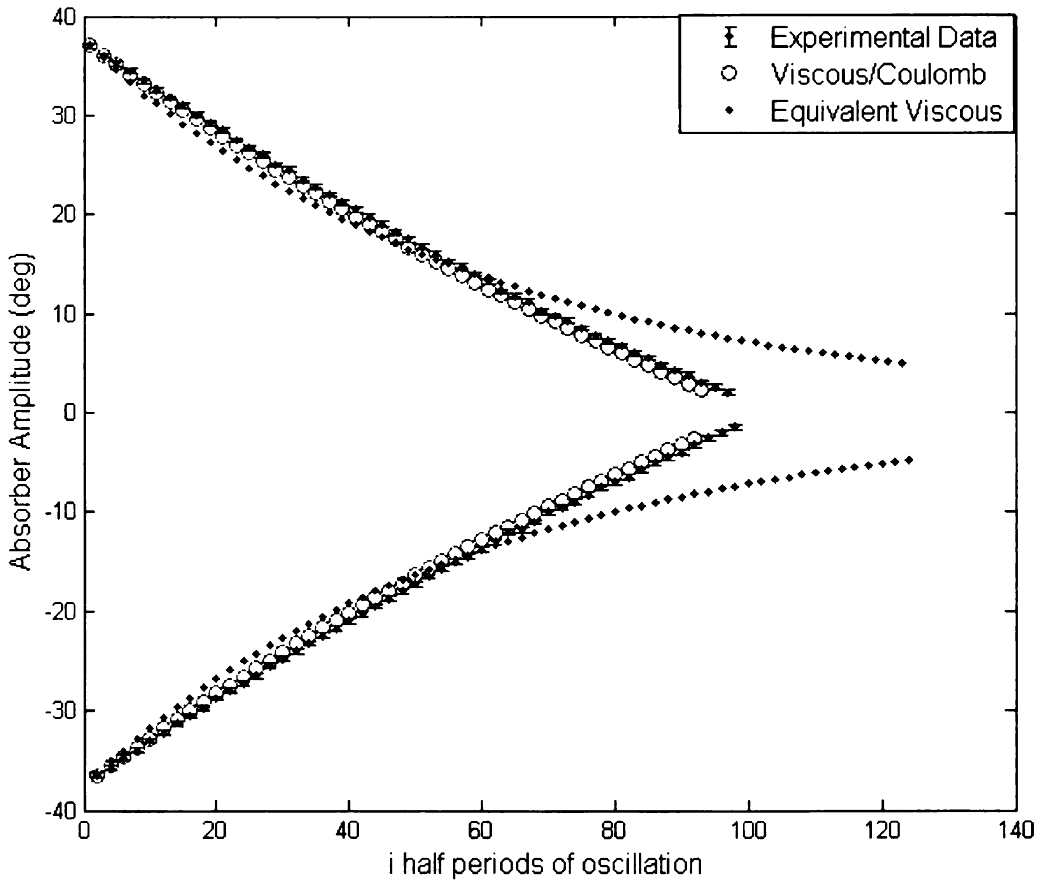

Figure 3.11: Theoretical vs. Experimental Free Vibration Peak Values for Large Amplitudes using the Damping Parameters Extracted from the Large Amplitude Decay for the Theory.

Figure 3.11. Theoretical vs. Experimental Free Vibration Peak Values for Large Amplitudes using the Damping Parameters Extracted from the Large Amplitude Decay for the Theory.

down as well as simulations using the viscous and Coulomb parameters extracted from the small amplitude decay. Also shown is the equivalent viscous response from the viscous parameter calculated in Figure 3.8.

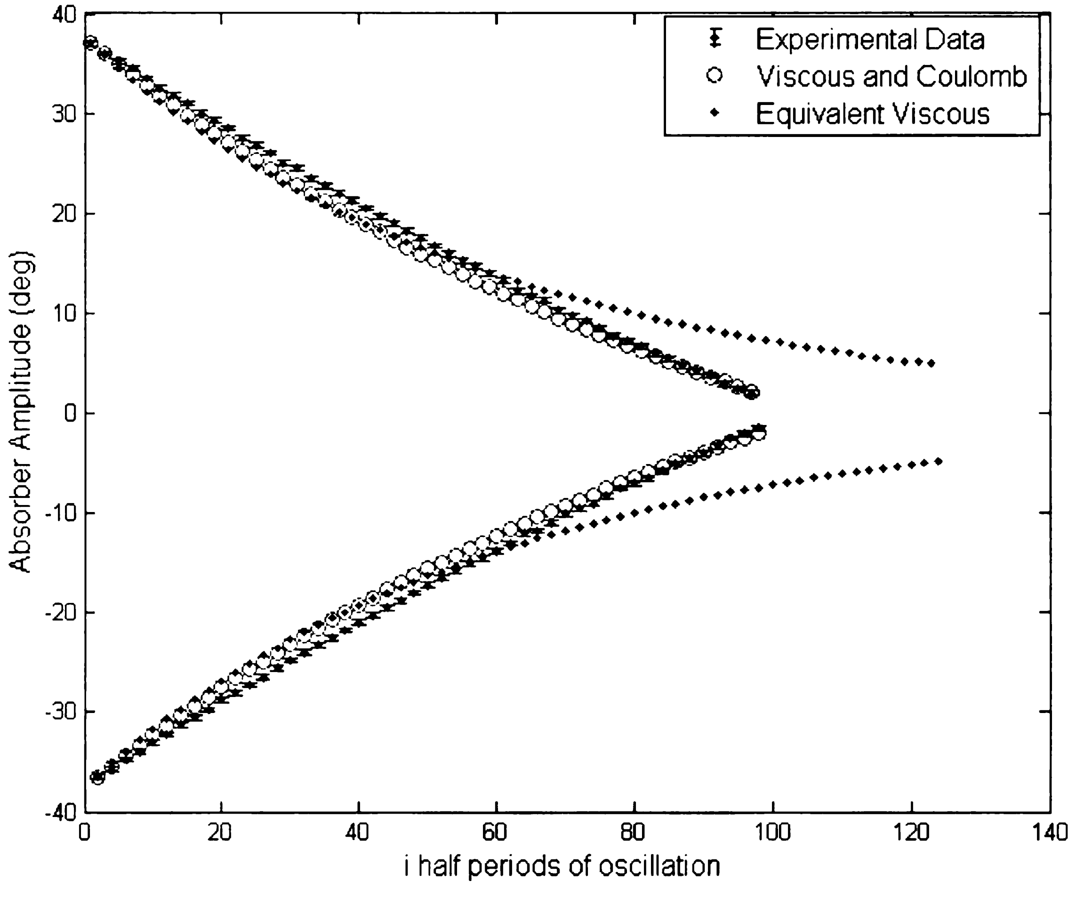

Figure 3.12: Theoretical vs. Experimental Free Vibration Peak Values for Large Amplitudes using the Damping Parameters Extracted from the Small Amplitude Decay for the Theory.

Examining Figure 3.12, the previous predictions about the response hold. The simulated response exhibits larger damping than the experimental results and then begins to track at around 10°. The simulations should begin to track around 16° though, and the reason for the late convergence is unknown.

Continuing to examine the discrepancies between the large and small amplitude

responses, one can impose the smaller amplitude portion of the large amplitude simulated response onto Figure 3.9. More precisely, maximum amplitude values from 16° to 0° were taken off the large amplitude simulation and imposed onto the small amplitude experimental data.

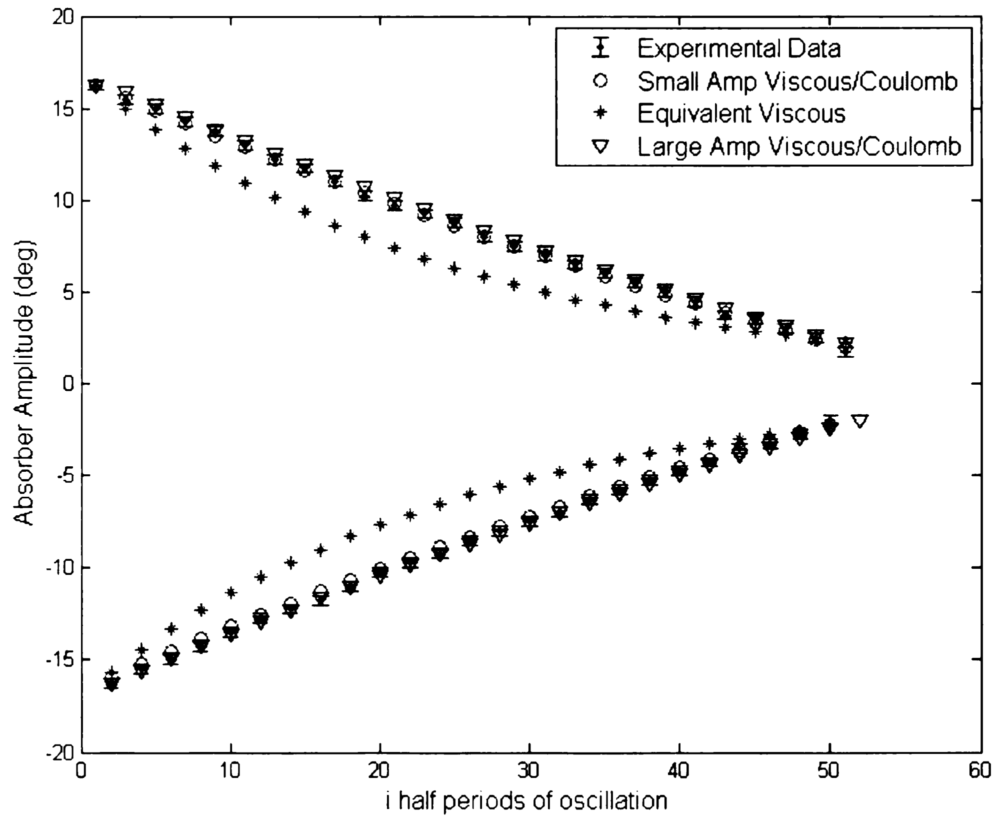

Figure 3.13: Theoretical vs. Experimental Free Vibration Peak Values for Small Amplitudes with Small Amplitude Simulation Data Extracted from the Large Amplitude Response.

The small amplitude data from the large amplitude simulation fits the small amplitude experimental data as expected. From this, one can conclude that the damping changed slightly between the two experimental tests. The reasons for this are unknown, and because the error is so small, the parameters extracted from the small amplitude decrement will be used for further analysis. A table containing all the

values estimated in this chapter is shown in Table 3.2.

Table 3.2: Values of Estimated Parameters.

Parameter	Value
R	0.118 m
L	0.039 m
m	0.225 kg
$\tilde{n}$	1.315
J	0.2678 kg·m^2
ϵ	0.0167
ρ	0.03377 m
x_k from small amplitude	0.1077
ζ from small amplitude	0.0025
x_k from large amplitude	0.1425
ζ from large amplitude	0.0014
ζ_{eq} small amplitude	0.0096
ζ_{eq} large amplitude	0.0051

Chapter 4

Steady-State Response: Theory and Experiments

The theory which was used to predict the absorber's steady state amplitude as well as the rotor angular acceleration will be compared to experimental results in this chapter. Simulations of the fully-nonlinear equations of motion are also imposed upon the experimental results. Experimental data presented contains error bars that arise from the error analysis described in Appendix A.

Using the same experimental setup detailed in Chapter 3, steady-state absorber amplitudes were recorded as the amplitude of fluctuating torque was varied. This test was run for several different detuning levels. Shown in Figure 4.1 is such a plot, conducted with 2% detuning ($n = 1.29$).

The full non-linear simulations and averaged equation qualitatively track the experimental results. At small absorber amplitudes, the experimental results show a lower absorber amplitude than theory predicts, then begin to follow the predicted response. The experimental results and the simulations jump at the same level of forcing, while the averaging theory predicts a slightly larger forcing to cause the instability. The hysteresis phenomenon is clearly exhibited in the experimental data:

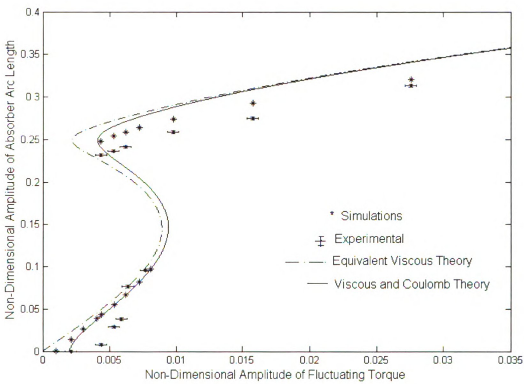

Figure 4.1: Non-Dimensional Absorber Arc Length vs. Non-Dimensional Amplitude of Fluctuating Torque for 2% Detuning. (a_{SS} vs. Γ)

sweeping up the torque causes the absorber amplitude to jump to the upper solution branch, and then while sweeping back down the absorber amplitude stays on the upper branch for smaller values of applied torque than initially caused the jump. Remembering that the absorber amplitude was scaled by ϵ, we can expect some error between the averaged equation response and the experimental and simulation results on the large amplitude solution. For this small level of detuning, the absorber jumps at a relatively low level of applied torque and causes an unwanted effect on the vibrations of the rotor. Figure 4.2 shows the angular acceleration of the rotor for the same conditions.

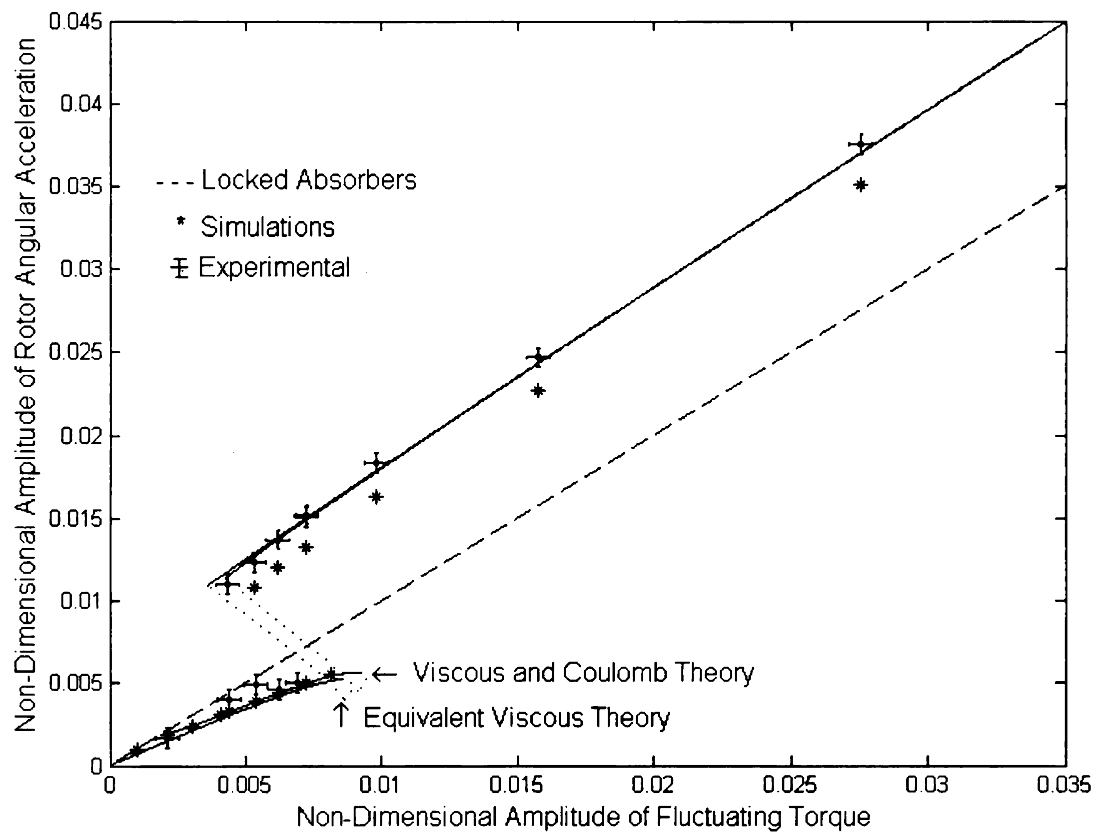

Figure 4.2: Non-Dimensional Rotor Angular Acceleration vs. Non-Dimensional Amplitude of Fluctuating Torque for 2% Detuning. ($\nu\nu'$ vs. Γ)

The experimental data in Figure 4.2 also tracks the theory nicely. One important feature to notice is the effect of the Coulomb friction causes the absorbers to stick at low forcing levels, and the angular acceleration of the rotor during this period is equal to that if the absorbers were locked. The Coulomb and viscous damping model predicts this and the first experimental data point fits almost exactly to the theory.

Once the absorbers lose stability and bifurcate to large amplitudes, they do indeed start increasing the torsional vibrations of the rotor as can be seen in Figure 4.2. In practice, this "jump" must be avoided and one can accomplish this by overtuning the absorbers. Shown in Figure 4.3 for 4% detuning is the absorber amplitude as a function of the applied torque.

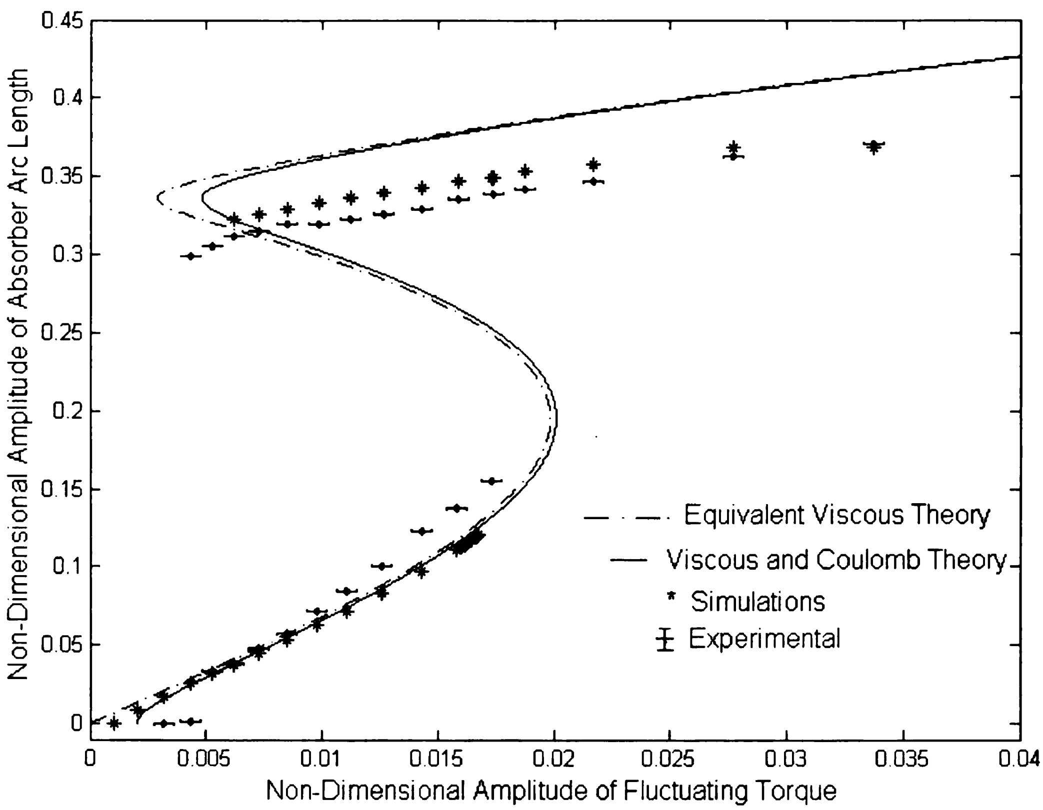

Figure 4.3: Non-Dimensional Absorber Arc Length vs. Non-Dimensional Amplitude of Fluctuating Torque for 4% Detuning. (a_{ss} vs. Γ)

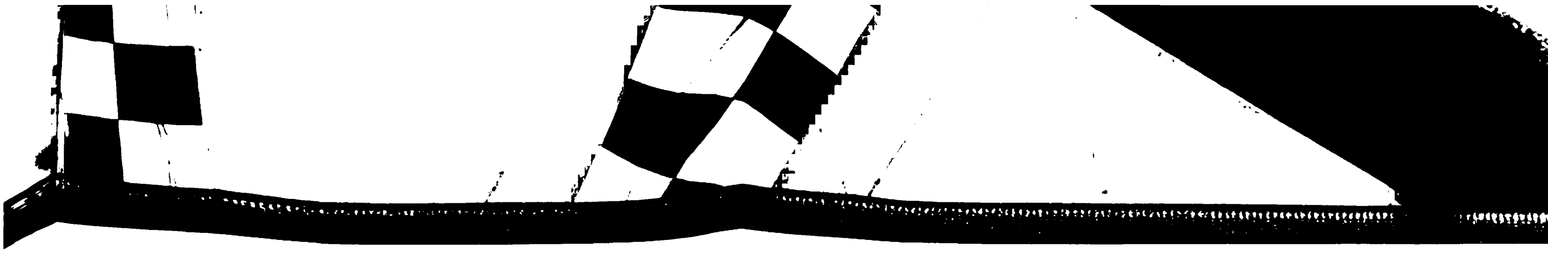

The experimental data confirm the theoretical prediction that the more overtuned the pendulum is, the more torque it takes to go unstable. As visible from Figure 4.3, the experimental results show the absorber sticking longer than theory predicts. One explanation for this could be that the static friction is larger than the kinetic friction in the experimental rig. Once the absorber becomes free, the experimental results follow the theory within the error bars until near the jump point. Nearing the jump bifurcation, the experimental and simulation data deviate slightly from the theory and becomes unstable at a torque level a little bit smaller than predicted. The bifurcation point can be difficult to capture exactly in experimentation, as the basin of attraction is so small the initial conditions could miss this basin. At low amplitudes the fully non-linear simulations quantitatively follow the averaged equations, thus confirming the accuracy of the averaged solution. Once the instability occurs, the simulations follow the experiments more closely than the averaging which is an effect of scaling the absorber amplitude. It has been extensively mentioned that the jump in absorber amplitude has an unwanted effect on its performance, and as one can see in Figure 4.4, the larger detuning level allows the absorber to counteract the applied torque for a greater range of forcing.

The final experimental results presented in Figure 4.5 are for a 6% level of detuning, in which one would expect it to take an even larger level of forcing to cause the absorbers to jump.

Once again, the insights gained from the theoretical analysis seem to hold when compared to the experimental results. At this large level of detuning, remembering that the averaged solution assumes forcing near the absorber tuning, one would expect the theory to deviate largely from the experimental results. This does not appear to be the case in this situation, and the theory and simulations follow the experimental results quite well on the lower branch.

Investigating Figure 4.6, the angular acceleration of the rotor is obviously reduced

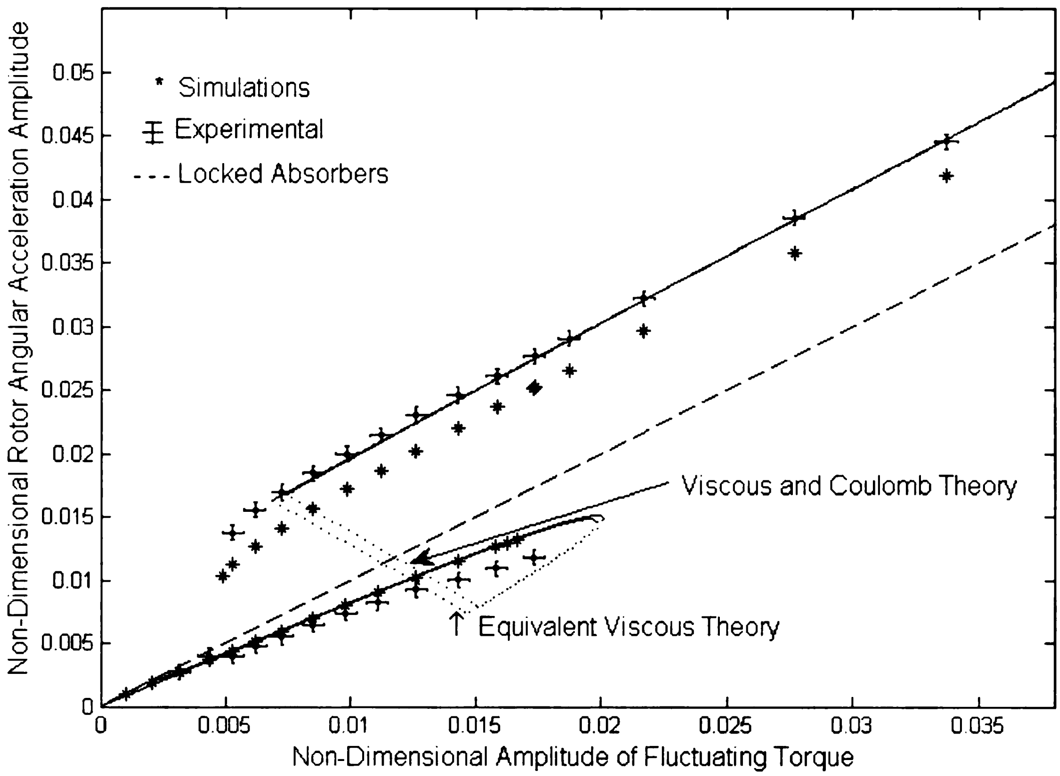

Figure 4.4: Non-Dimensional Rotor Angular Acceleration vs. Non-Dimensional Amplitude of Fluctuating Torque for 4% Detuning. ($\nu\nu'$ vs. Γ)

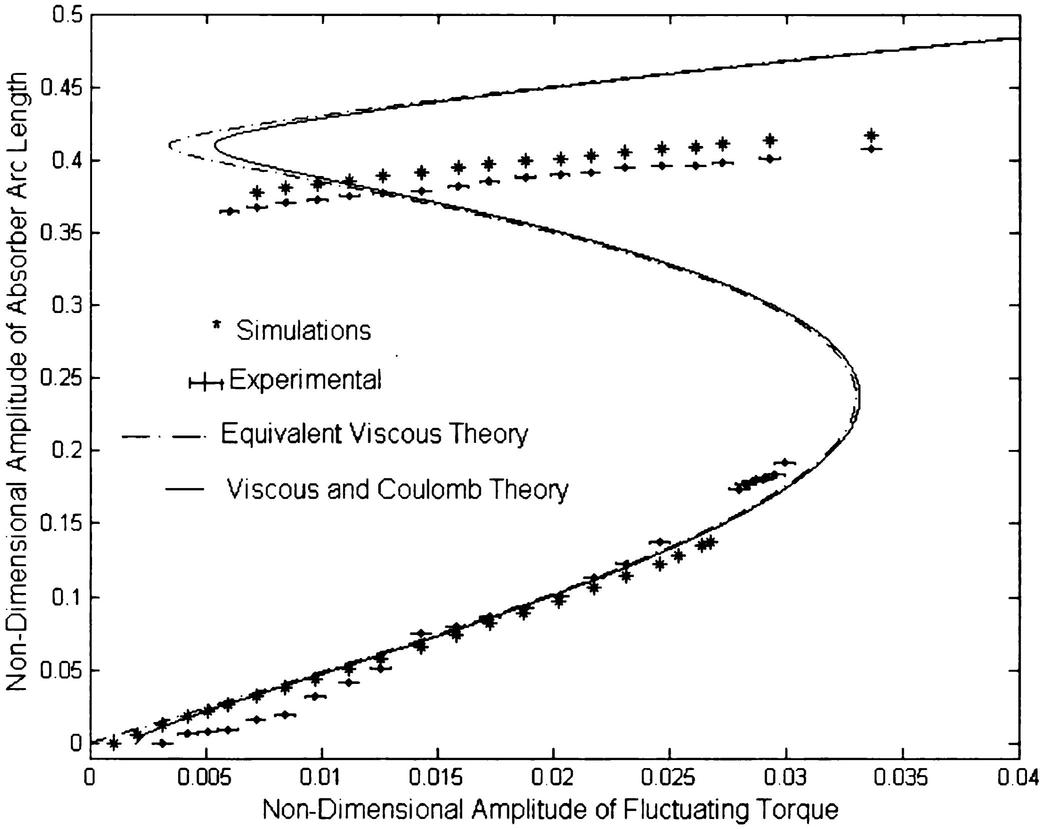

Figure 4.5: Non-Dimensional Absorber Arc Length vs. Non-Dimensional Amplitude of Fluctuating Torque for 6% Detuning. (a_{SS} vs. Γ)

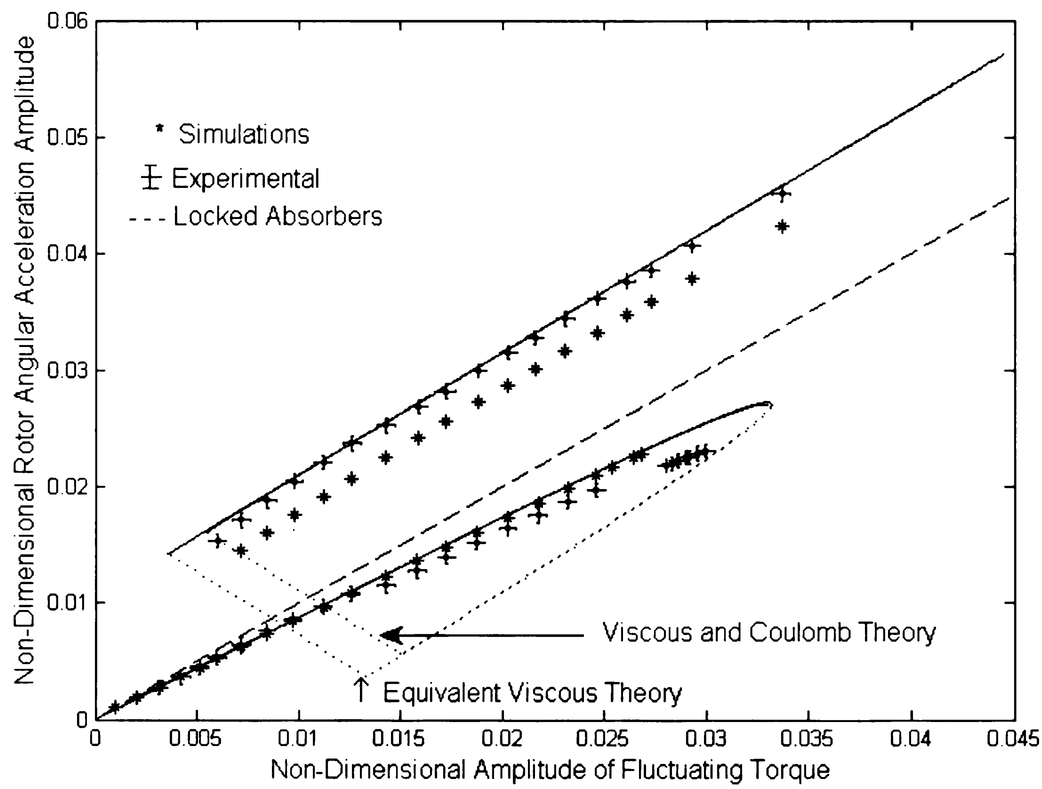

Figure 4.6: Non-Dimensional Rotor Angular Acceleration vs. Non-Dimensional Amplitude of Fluctuating Torque for 6% Detuning. ($\nu\nu'$ vs. Γ)

via the oscillation of the absorber. The amount reduced for the large detuning level is less than that in the previous plots for smaller detuning levels, but has the benefit of remaining stable for much larger ranges of fluctuating torque.

Chapter 5

Conclusions and Recommendations for Future Work

In Chapter 2, the equations of motion for a single CPVA attached to a rotor were scaled and averaged with the inclusion of a Coulomb friction term, which led to some initial theoretical investigation into the effects of parameters on the dynamics of the system. The pendulums were found to bifurcate to large amplitudes at a certain level of forcing with the undesired effect on the performance of the absorbers that the instability causes. The effect of the Coulomb friction was shown to cause the absorbers to stick for very small levels of forcing as well as predicting it to take a larger value of fluctuating torque to cause the absorbers to jump.

The experimental spin rig was introduced and different sets of test were conducted to identify certain parameters associated with the rig. The simultaneous viscous/Coulomb decrement scheme was shown to accurately identify the respective parameters on the test rig in the presence of noise. It was noted that the damping in the rig seemed to change slightly from test to test and the reason for this is not fully understood. With this being said, the amount the parameters seemed to change was very small, and the damping parameters estimated were believed to accurately

capture the actual damping in the system.

The experimental results presented in Chapter 3 confirmed qualitatively and at times quantitatively the theory previously developed. The sudden jump in absorber amplitude was captured experimentally and the effect that detuning has on the absorbers was also observed. The validity of the averaged equations was confirmed via simulations of the fully non-linear equations of motion. The Coulomb friction term seemed to have a greater effect on the small amplitude performance of the absorber as well as lower detuning levels. The effect at lower amplitudes was expected as the Coulomb friction term dominates over the viscous term at small amplitudes of oscillation.

At large values of detuning (6%), the theory surprisingly predicted the experimental results quite accurately. Recalling that the detuning parameter, σ, was scaled to order ϵ, one would expect the averaging to lose some validity at such a large level of detuning.

Overall, correctly identifying the damping parameters leads to a more accurate prediction of the performance of the at low forcing and corresponding low absorber levels. Once the absorber jumps, the equivalent viscous model and the Coulomb/viscous model converge onto each other and their difference is negligible.

5.1 Recommendations for Future Work

With this work, coupled with that of Nester [9], the steady-state response of a single, circular path absorber has been extensively studied and no recommendations for further work on this are necessary. With regards to circular path absorbers, and especially ones for use in automotive applications, the transient response of the absorbers should be investigated more thoroughly. As the engine starts and stops, as well as transitions between full and half cylinder mode in multi-displacement engines,

the absorbers are in a transient phase and amplitude overshoots are common. These overshoots can potentially be dangerous and affect the performance of the absorber.

Nester also investigated multiple absorbers attached to a rotor and experimentally observed non-synchronous behavior that cannot yet be explained. Some research into explaining these experimental results would be well worth the work.

With research conducted into alternative absorber paths (epicycloid,cycloid) [4, 12]which have been found to alleviate the the jump instability, circular path absorbers should be considered only for ease of manufacturing. Therefore, quantifying the damping parameters, investigating transient and non-synchronous responses should all be conducted experimentally for non-circular path absorbers. Suspending the absorbers from the rotor in a bifilar fashion (see Figure 5.1) has been a common approach for allowing the absorbers to follow specific paths.

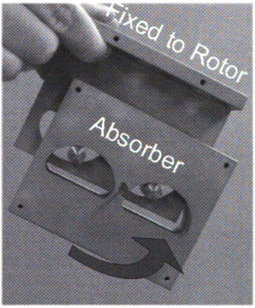

Figure 5.1: Photo of a Bifilar Absorber

In the bifilar design, two identical curves are cut out on a carrier attached to the rotor as well as two identical, but inverted curves on the pendulum. Two cylindrical

rollers roll along these curves, allowing the pendulum to translate but not rotate. Since the rollers rotate and translate, their dynamics can be a factor and these dynamics were first investigated by Denman [4], who included the rollers in the equations of motion. Monroe et. al [11] recently investigated the effect the rollers have on the non-linear tuning of bifilar absorbers and obtained a tautochronic path for non-zero roller inertias. Bifilar absorbers were experimentally tested on a rotor spinning in the horizontal frame. An out of plane instability was observed, and created problems when attempting to quantify the damping parameters. These absorbers should be tested in the vertical plane, which is assumed to alleviated the out of plane instability.

Chapter 6

Appendix A

In this appendix we will attempt to quantify the experimental measurement error in the CPVA testing device. The main measurements of interest include:

1. Absorber COM position s
2. The speed of the rotor $\dot{\theta}$
3. The applied torque which includes the mean T_0 and fluctuating T_θ (at order of interest),

where the position of the absorber(s) and the rotor speed are each measured with an encoder. The applied torque on the rotor is measured from a feedback current that the motor outputs. Each of these measurements will be discussed in more detail in the following sections. This document follows the NIST experimental uncertainty guidelines which are published online and in a document.

Uncertainty in Absorber position: A U.S. Digital optical encoder is used to measure absorber position. These encoders contain 4 channels which are A, -A, B, and -B. The two negative channels are literally the negative of A and B, respectively. To eliminate the noise in the encoder signal the positive channel is subtracted from the negative channel and then divided by 2. The encoder has 360 pulses per revolution,

meaning that with 4 channels we get $\frac{1}{4}$ degree resolution from this encoder. Therefore, assuming the pulses are equally spaced on the encoder and we don't miss any counts, the uncertainty in the absorber position is

$$u_S = \pm\frac{1}{4}. \tag{6.1}$$

Speed of rotor: The encoder on the rotor has 1000 pulses per revolution which are fed into a frequency to voltage (F2V) converter. The F2V converter measures the instantaneous frequency between two pulses in pulses/sec. This frequency is divided by 1000 to obtain the frequency of the rotor in Hz. This device is rated to be able to measure up to 25 kHz between pulses which means approximately 25 Hz for 1000 pulses. An important check here was to make sure the F2V converter could detect the frequency of the rotor during a torsional disturbance. This means the rotor is now rotating at a mean speed with a oscillating part superimposed. In terms of pulses going into the F2V this means that these pulses are no longer evenly spaced along the time axis. Now their time spacing is modulated (i.e. they get closer and further apart, etc.) due to the fluctuation about the mean rotor speed. The bandwidth of the F2V converter turned out to be sufficiently large to resolve the frequency of the rotor pulses. Using the specification sheet from the device manufacturer, the accuracy calibration of the device is given as a maximum ±0.1% of the frequency span to be measured. Since the frequency at the tuning order for the absorbers used in our lab is about 10 Hz for mean speeds at 400 rpm, an estimate for the uncertainty in the F2V conversion using a 10 Hz span which corresponds to an output voltage of 3V (of the 5 V range) is

$$u_{\dot{\theta},F2V} = \pm(3v)(.001) = \pm 3mV. \tag{6.2}$$

After the signal leaves the F2V converter it is digitized by the national instruments DAQ board (PCI-6281). According to the spec sheet, the device has an absolute

accuracy of 1.05 mV with the built-in low pass filter turned off. The quantization step size for the 18 bits at $\pm(10v)$ range is

$$Q_{NI} = \frac{2*(10v)}{2^{18}-1} = 7.6294*10^{-5}V. \tag{6.3}$$

To obtain the quantization error from this we divide Q in half because at worst our actual signal amplitude could have been exactly in the middle of the quantization step (i.e. Q/2), in which case it would be rounded up and anything below is rounded down. Note that this also assumes the maximum amplitude of our signal is approximately 10 volts which is the maximum analog input voltage to the DAQ board. Although, this isn't always the case, we will approximate the quantization error as

$$Q_{NI,error} = Q_{NI}/2 = \pm 0.0381mV. \tag{6.4}$$

Since the quantization error is about 3% of the absolute accuracy given in the NI DAQ specification sheet, we will assume that the quantization error was accounted for in this specification. Therefore the uncertainty in digitizing the speed signal u_{DAQ} is

$$u_{\dot{\theta},DAQ} = \pm 1.05mV. \tag{6.5}$$

Finally, the last bit of uncertainty is the overall noise floor of the signal's FFT. This can be determined simply by taking an FFT of the speed signal in Labview and then plotting the magnitude of the Fourier coefficients. One then estimates the largest amplitude at which white is present (i.e. constant amplitude level at all frequencies). This is determined to be

$$u_{\dot{\theta},FFT} = \pm 0.02mV. \tag{6.6}$$

The total uncertainty in the rotor speed is

$$u_{\dot{\theta},T} = u_{\dot{\theta},F2V} + u_{\dot{\theta},DAQ} + u_{\dot{\theta},FFT} = \pm 3.07mV. \tag{6.7}$$

Torque Uncertainty: The torque measurement comes from a current feedback signal that is multiplied by two calibration constants (see ultraware software) to convert the units of the signal to Newton-Meters. This signal is digitized by the gray control box and the national instruments DAQ board. The quantization for the gray control box which is 8 bits at a $\pm(10v)$ range is

$$Q_{box} = \frac{2 * (10v)}{2^8 - 1} = 78.43mV. \tag{6.8}$$

Just like before we can approximate the quantization error as

$$Q_{box,error} = Q_{box}/2 = \pm 39.22mV. \tag{6.9}$$

Digitizing the torque signal with the National Instruments DAQ board will have the same uncertainty as calculated in equation (6.5). Similar to the rotor speed signal, the white noise level for the torque signal is estimated in the same way. This uncertainty is found to be

$$u_{T_\theta,FFT} = \pm 2mV. \tag{6.10}$$

The total uncertainty in the torque signal is

$$u_{T_\theta,T} = u_{\dot{\theta},DAQ} + Q_{box,error} + u_{T_\theta,FFT} = \pm 42.27mV. \tag{6.11}$$

Combined Uncertainties for the Rotor Angular Acceleration and Rotor Inertia: Using the uncertainties above, this section computes the combined uncertainty for the rotor acceleration and the rotor inertia.

Rotor Angular Acceleration: The rotor angular acceleration at order n is computed as follows

$$\ddot{\theta}_n = n\Omega\dot{\theta}_n, \tag{6.12}$$

where n is order of excitation, Ω is the mean speed that the fluctuation is about, and $\dot{\theta}_n$ is the magnitude of the FFT of the rotor speed signal at order n. Assuming the fluctuations in Ω and $\dot{\theta}_n$ are uncorrelated, the combined uncertainty for $\ddot{\theta}_n$ is computed following the NIST standards as follows:

$$u^2_{\ddot{\theta}_n} = \left(\frac{\partial\ddot{\theta}_n}{\partial n}\right)^2 u^2_n + \left(\frac{\partial\ddot{\theta}_n}{\partial\Omega}\right)^2 u^2_\Omega + \left(\frac{\partial\ddot{\theta}_n}{\partial\dot{\theta}_n}\right)^2 u^2_{\dot{\theta}_n}. \tag{6.13}$$

We assume here that there is no error in the order of the torque signal $u_n = 0$ which is generated in Labview. To estimate error in the ability of the PID to maintain a constant speed (u_Ω), an experiment is run with the rotor spinning at a constant rate with PID active. The mean and standard deviation of the resulting rotor speed signal is computed using basic statistics and the standard deviation yields u_Ω which is

$$u_\Omega = \pm 2.39mV. \tag{6.14}$$

The uncertainty in the rotor speed at order n ($u_{\ddot{\theta}_n}$) had already been calculated in equation (6.7). Taking the derivatives in equation (6.13) and using equations (6.14) and (6.7), the uncertainty in the angular acceleration at order n is

$$u^2_{\ddot{\theta}_n} = (n\dot{\theta}_n)^2 u^2_\Omega + (n\Omega)^2 u^2_{\dot{\theta},T}, \tag{6.15}$$

which will provide error bars on a $\ddot{\theta}_n$ measurement of $\pm u_{\ddot{\theta}_n}$.

Rotor Inertia: To compute the rotor inertia we use Newton's law to obtain

$$J = \frac{T_{\theta_n}}{\ddot{\theta}_n}, \tag{6.16}$$

where T_{θ_n} is the magnitude of the applied fluctuating torque at order n and $\ddot{\theta}_n$ is the angular acceleration of the rotor at order n calculated according to equation (6.12). Assuming the fluctuations in T_{θ_n} and $\ddot{\theta}_n$ are uncorrelated, the uncertainty in the rotor inertia is

$$u_J^2 = \left(\frac{1}{\ddot{\theta}_n}\right)^2 u_{T_{\theta_n}}^2 + \left(\frac{T_{\theta_n}}{\ddot{\theta}_n^2}\right)^2 u_{\ddot{\theta}_n}^2, \tag{6.17}$$

where $u_{T_{\theta_n}}$ and $u_{\ddot{\theta}_n}$ are the uncertainties calculated in equations (6.11) and (6.15), respectively. The error bars on the rotor inertia calculation will then be $\pm u_J$.

BIBLIOGRAPHY

[1] Abdallah Saleh Alsuwaiyan. *Performance, Stability, and Localization of Systems of Vibration Absorbers.* PhD thesis, Michigan State University, 1999.

[2] J.V. Beck and K.J Arnold. *Parameter Estimation.* Wiley, 1977.

[3] C. P. Chao and S. W. Shaw. The dynamic response of multiple pairs of subharmonic torsional vibration absorbers. *Journal of Sound and Vibration*, 231:411–431, 2000.

[4] H. H. Denman. Tautochronic bifilar pendulum torsion absorbers for reciprocating engines. *Journal of Sound and Vibration*, 159:251–277, 1992.

[5] J. P. Den Hartog. *Mechanical Vibrations.* Dover Publications, Inc. New York, 1985.

[6] KerWilson. *Practical Solutions of Torsional Vibration Problems.* Chapman and Hall, Ltd., London, 1968.

[7] J. W. Liang and B. F. Feeny. Identifying coulomb and viscous friction from free-vibration decrements. *Nonlinear Dynamics*, 16:337–347, 1998.

[8] J. Madden. Constant frequency bifilar vibration absorber. Technical report, United States Patent No. 4218187, 1980.

[9] Tyler M. Nester. Experimental investigation of circular path centrifugal pendulum vibration absorbers. Master's thesis, Michigan State University, 2002.

[10] D. E Newland. Nonlinear aspects of the performance of centrifugal pendulum vibration absorbers. *ASME Journal of Engineering for Industry*, 86:257–263, 1964.

[11] A. H. Haddow B. K. Geist R. J. Monroe, S. W. Shaw. Accounting for roller dynamics in the design of bifilar torsional vibration absorbers. In *Proceedings of the ASME 2009 International Design Engineering Technical Conferences & Computers and Information in Engineering Conference*, San Diego, CA, 2009.

[12] Peter Schmitz. Experimental investigation into epicycloidal centrifugal pendulum vibration absorbers. Master's thesis, Michigan State University, 2003.

[13] A.G. Haddow S.W. Shaw, M.B. Orlowski and B. Geist. Transient dynamics of centrifugal pendulum vibration absorbers. In *Proceedings of the 12th International Symposium on Transport Phenomena and Dynamics of Rotating Machinery*, number 2008-20119, Honolulu, HA, 2008.

[14] S.W. Shaw J.E. Brevick & V.J. Borowski T.M. Nester, A.G. Haddow. Vibration reduction in variable displacement engines using pendulum absorbers. In *Proceedings of the SAE Noise and Vibration Conference and Exhibition*, 2003.